Photon-sail periodic orbits around the Lagrange points of the Alpha-Centauri system

Master of Science Thesis

Luc Haagh

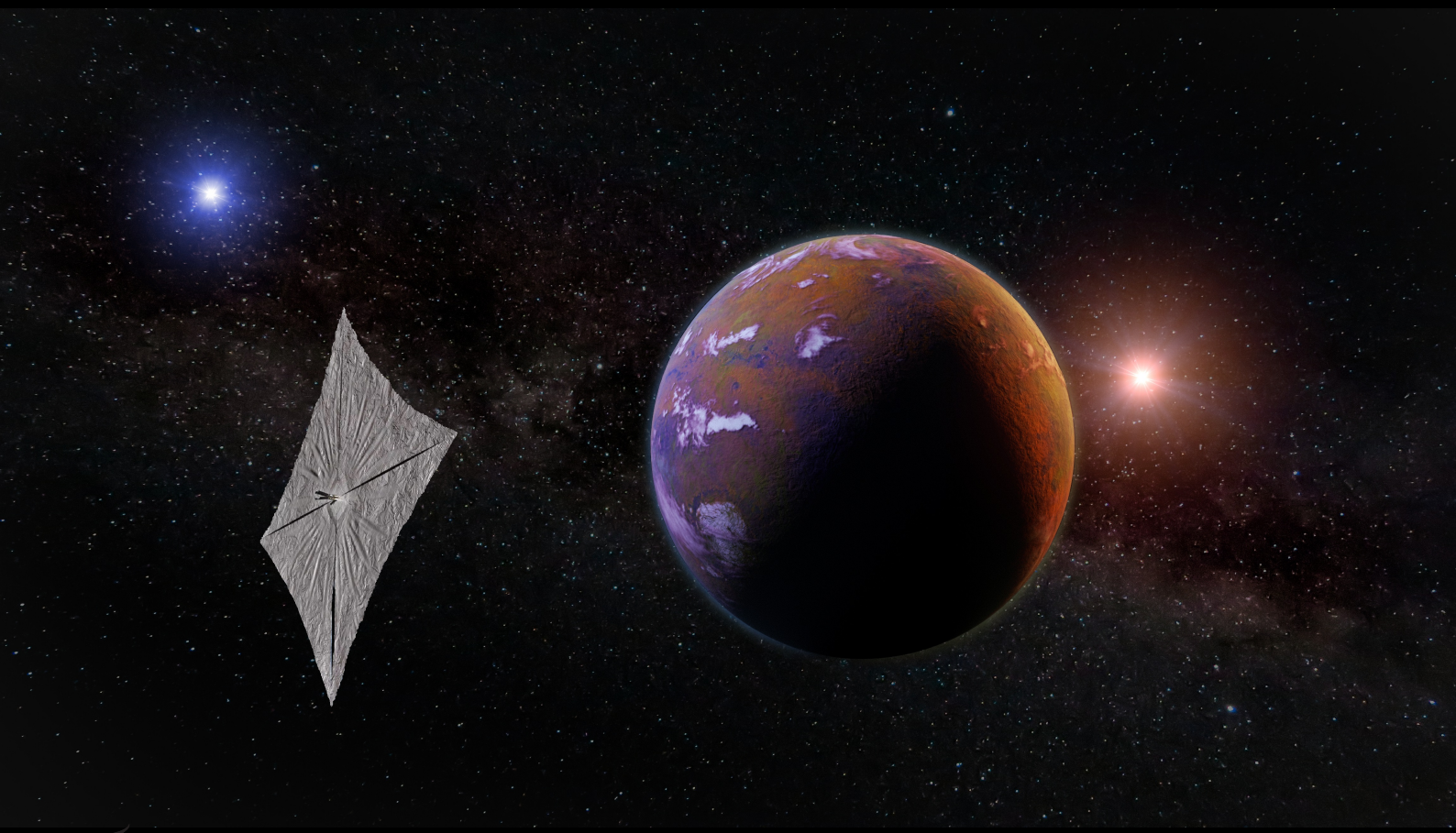

TU Delft

Photon-sail periodic orbits around the Lagrange points of the Alpha-Centauri system

Master of Science Thesis

by

Luc Haagh

to obtain the degree of Master of Science
at the Delft University of Technology,
to be defended publicly on Wednesday August 16, 2023 at 14:00 PM.

Student number:	4550366	
Thesis committee:	Dr. ir. M.J. (Jeannette) Heiligers	TU Delft, daily supervisor
	Ir. R. (Ron) Noomen	TU Delft, internal examiner
	Prof. Dr. Ir. P.N.A.M. (Pieter) Visser	TU Delft, chair
	S. (Stefano) Speretta	TU Delft, external examiner

Cover page credits: iStock, Planetary Society
https://www.gettyimages.nl/detail/foto/beautiful-exoplanet-part-of-an-alien-binary-star-royalty-free-beeld/918027292
https://www.planetary.org/sci-tech/lightsail

TU Delft

Preface

I have been interested in the exploration of space ever since I was a young boy. So, after finishing the BSc Aerospace Engineering I quickly determined that the Master track 'Space Exploration' would be the next step. After getting introduced to the concept of photon sailing, I started exploring the possibilities of writing my thesis on this subject. The futuristic idea of exploring other stellar systems has been in my imagination for a long time which made the choice of applying the concept of sailing in the Alpha-Centauri system an easy one to make. After a lot of work in the past months, this work represents the end of my study career and marks the start of my working career.

I could not have achieved this by myself and therefore I want to thank some people. First and foremost, I want to thank Jeannette Heiligers, who was my daily supervisor during the thesis. I am really thankful for the weekly meetings we had which always pushed me in the right directions if I ran into a problem. During these, I was often amazed about all the knowledge she had regarding photon sailing and the numerical methods I have used. She also organised a weekly meeting with fellow students working on photon sailing in their theses. These students also helped me a lot by having a critical view during the progress presentations, but also gave an encouraging feeling when things were not going as planned. Therefore, I want to thank my fellow students for their time and enthusiasm during these weekly meetings.

I also want to thank my friends who supported me when I was working, but also distracted me during the days off. Last but not least, I want to thank my roommate and parents who often asked how the process with all the 'weird circles' was going, which they saw on my screen. During these daily coffee breaks with my parents or roommate, I often got the energy back to continue working on my thesis.

Luc Haagh
Delft, August 2023

Executive Summary

This thesis investigates the existence of periodic orbits in the Alpha-Centauri (α-Cen) system with the use of a photon sail. These periodic orbits are designed around the classical Lagrange points and stay in the plane of motion of α-Cen A and B, also called planar Lyapunov orbits. In this research, only the colinear Lagrange points, namely L_1, L_2 and L_3 are taken into consideration. The α-Cen system is the stellar system closest to our own, at a distance of 4.37 lightyears. It is a triple-star system, with α-Cen A and B in binary motion. The third and smaller star Proxima Centauri orbits this inner binary system. The system also includes a few confirmed (possibly habitable) exoplanets. Both the relative proximity and the exoplanets that are present in the system make it a scientifically very interesting destination for the first interstellar mission.

Planar Lyapunov orbits have been designed in other systems before. Examples of such systems are the Earth-Moon and Sun-Earth systems. These systems have been modelled as a restricted three-body problem, which contains two large bodies and one body with a negligible mass. For systems where the two primaries orbit in (almost) circular motion, the circular restricted three-body problem (CR3BP) is mostly used, while the elliptical restricted three-body problem (ER3BP) is used for systems with elliptical motion. In the case of α-Cen, the two primaries orbit their barycenter in a very elliptical orbit with an eccentricity of $e = 0.5208$. Therefore, the ER3BP is used as a basis in this research to model the binary system of α-Cen. In this model, α-Cen A and B are the two primary bodies and the spacecraft is the third body with a negligible mass. At periastron, Proxima Centauri has a distance of approximately 4300 AU to the barycenter of the system. The maximum distance of α-Cen A and B to the barycenter is approximately 36 AU. Therefore, it is assumed that the photogravitational effect of Proxima Centauri can be neglected.

In mission designs to travel towards α-Cen, photon-sail acceleration is a frequently used method of propulsion due to the continuous photon radiation pressure on the sails. Therefore, research has already been conducted on the photon-sail dynamics in the α-Cen system itself. Examples of such research are identifying artificial equilibrium points and designing trajectories between the equilibrium points. The photon-sail acceleration adds an extra term to the equations of motion of the ER3BP. The magnitude of the photon-sail acceleration depends on the lightness number of the sail. The lightness number is a parameter which quantifies the performance of the sail, as it is defined as the ratio of the photon-sail acceleration over the gravitational acceleration. Due to the addition of the photon sail in the model, the photon-radiation pressure (PRP) augmented ER3BP is used to design the planar Lyapunov orbits. In this report, photon radiation pressure is used as a general term for solar radiation pressure, as the latter only applies for the emitted radiation from the Sun.

A multiple shooting differential correction (MSDC) algorithm is used to design the planar Lyapunov orbits. As an initial guess, the spacecraft at the Lagrange point is perturbed in the direction of the eigenvector associated to the imaginary eigenvalue of the linearised equations of motions (EoM) in the CR3BP. This perturbed spacecraft is propagated until it crosses the line between the two main bodies again. The MSDC divides the initial trajectory in multiple segments with patch points between the segments and tries to make the entire orbit continuous in two levels. The first level corrects the velocity of each patch point in order to reach the next patch point. This is done by propagating the trajectory and the state transition matrix (STM) forward. The STM linearly approximates the change in the state at the end of the propagation when changing the state at the beginning of the propagation. With the STM, an approximation is made of the required change in the initial velocity to reach the next patch point. The MSDC continues with changing the initial velocity until the difference between the final position of the propagation and the position of the next patch point is smaller than 10^{-9} in dimensionless units. With such small differences, it is assumed that the trajectory is continuous in terms of position. The second level of the MSDC tries to make the trajectory continuous in velocity by changing the positions of the patch points. Using the STM, the velocity difference at a certain patch point is

minimised by relocating the previous patch point, the patch point with the velocity difference itself and the following patch point. After relocating all patch points of the trajectory once, the first level is activated again. This iterative process continues until the norm of all velocity differences is smaller than 10^{-4} in dimensionless units.

Due to the eccentricity of the system, the equations of motions are dependent on the true anomaly of the system. To ensure periodicity of the orbit, the period of each orbit should be 2π or a fraction of that. This adds an extra constraint to the design of the periodic orbit. This makes it hard for the MSDC to converge the initial guess to a periodic orbit in the PRP-augmented ER3BP. Therefore, the initial guess is made in the CR3BP which is used to design a family of periodic orbits with varying periods. The orbits with periods of $\frac{2\pi}{n}$, where n is an integer, are used as input in the ER3BP. In small steps, the eccentricity is increased until it reaches a value of $e = 0.5208$. After that, the lightness number is also increased until the MSDC can not converge the trajectory to a periodic orbit. In this way, families of PRP-augmented planar Lyapunov orbits are derived with increasing lightness numbers up to a defined $\beta_{max} = 2$.

There are three different results depending on the orientation of the sail when increasing β. First of all, the periodic orbit can shrink in size for larger lightness numbers. If the sail is placed in such a way that the PRP acceleration keeps relatively high, the orbit will continue to shrink until the maximum velocity V_{max} converges to 0, which means that an artificial equilibrium point (AEP) will be created. This means that, independent of the orientation, β_{max} is equal to the lightness number required to create an AEP close to one of the stars. For α-Cen A, this means that $\beta_{max} \approx 0.727$ and for α-Cen B that $\beta_{max} \approx 1.86$. Another option is that when the periodic orbit is shrinking, that the effect of the photon sail is decreasing. This is achieved when the normal vector of the sail is pointed perpendicular to the photon rays when the spacecraft is in between the two stars. The smaller orbits stay close to the line between α-Cen A and B, so the effect of the sail is minimised. Therefore, V_{max} converges to a constant value greater than 0, which means that $\beta_{max} = 2$. Lastly, if the PRP acceleration is too small or too large, the periodic orbit will expand, resulting in V_{max} going to infinity. Therefore, β_{max} is achieved at the vertical asymptote of V_{max}. Lyapunov orbits around L_2 and L_3 in the classical ER3BP with an initial true anomaly of 0 are very close to the primary bodies. Therefore, V_{max} tends to go to infinity for most orientations except for the orientation where the normal vector is always placed parallel to the photon rays of the closest star. In this case, the orbit converges to an AEP. If the initial true anomaly is changed to π, the orbit is further away from the stars, resulting in more orientations reaching $\beta_{max} = 2$.

To further explore α-Cen, trajectories between two planar Lyapunov orbits are designed. Using the adaptive differential evolution (JADE) algorithm, a population of vectors evolves over generations. Each individual of the new generation is compared to the previous generation and the best individual remains. The JADE algorithm is more elaborate compared to the standard differential evolution algorithm. The crossover probability parameter is adapted over the different generations, making this parameter less problem-dependent. The trajectory is divided into a departure and arrival leg and the JADE algorithm tries to minimise the Euclidean error between the states at the ends of these legs. The lightness number of the sail during the trajectory is set to $\beta = 0.1$, 0.5 and 2 to investigate its effect. For $\beta = 0.1$, the Euclidean error is relatively high at a dimensionless value in the range of 1E-1 to 1E-3, depending on the chosen Lyapunov orbits. For $\beta = 0.5$ and 2, the Euclidean error is negligible which means that the trajectory can be assumed to be continuous. The time of flight (TOF) of the trajectory for $\beta = 2$ is almost 25% lower compared to the trajectory for $\beta = 0.5$.

Only five different steering laws were used to identify the planar Lyapunov orbits. These orientations resulted in a maximum PRP acceleration if $\alpha = 0$ deg or a minimum PRP acceleration for $\alpha = 90$ deg. Therefore, it is reccommended to further investigate the orientations between these boundary conditions to get an overview of the possible orientations to reach $\beta_{max} = 2$. The tipping points between the three options when increasing the lightness number can give more insight in the PRP-augmented dynamics of α-Cen. Next to that, it is recommended to use a time-constrained MSDC algorithm to decrease the TOF of the trajectories between the Lyapunov orbits. Using the continuation method to slowly decrease the constrained TOF will result in a smaller TOF.

Contents

Nomenclature

Abbreviations

AEP	Artificial equilibrium point
AU	Astronomical unit
CR3BP	Circular restricted three-body problem
EoM	Equations of Motion
ER3BP	Elliptic restricted three-body problem
JADE	Adaptive differential evolution
L_1, L_2, L_3	Colinear Lagrange points
MSDC	Multiple shooting differential correction
PRP	photon-radiation pressure
STM	State transition matrix
TOF	Time of flight
α-Cen	Alpha-Centauri

Symbols

e	Eccentricity
L	Luminosity
M	Mass
R	Radius
V_{max}	Maximum magnitude of velocity
β	Lightness number
θ_0	Initial true anomaly of Alpha-Centauri
μ	Dimensionless mass of α-Cen B
Φ	State transition matrix
$\odot$	Sun

List of Figures

List of Tables

1 Introduction

Humanity has been gazing into the sky for centuries wondering what is out there. Since the 20th century, the first spacecraft have been launched to explore the space around us, starting with orbits around our own Earth and eventually exploring our entire Solar System. The next step in the exploration of humanity is expected to be travelling to another stellar system. With the use of a futuristic photon sail, it can be possible to visit the α-Centauri system within a lifetime. In this research, the dynamics of a photon sail within the α-Centauri system is investigated as a basis for a future mission towards our closest neighbour.

1.1. History of photon sailing

The first concepts of photon sailing can be traced back to the 17th century when Johannes Kepler observed the trail of a comet, which he thought to be caused by the Sun. He imagined that a spacecraft with a large sail could use these forces as a method of propulsion. Later, Maxwell published his theory that light has momentum, which means that it can exert a force on an object [4]. Throughout the early 20th century, scientists like Konstantin Tsiolkovsky and Fridrikh Tsander extended the thought of photon sailing and performed important theoretical research [5]. Tsiolkovsky envisioned the use of large mirrors to reflect sunlight onto spacecraft sails, while Tsander proposed employing thin metal foils to capture the Sun's radiation. At the end of the 20th century, the first photon sail missions were proposed to rendezvous with Halley's comet [6]. At this time, the first experiments were conducted to validate the feasibility of the technology.

The first launch of a photon sailcraft was a major milestone. In 2010, the Interplanetary Kitecraft Accelerated by Radiation of the Sun (IKAROS) was launched by the Japanese Aerospace Exploration Agency (JAXA). IKAROS successfully deployed its sail and demonstrated the first successful application of photon sailing. The sail deployed in space is shown in Figure 1.1a. The IKAROS mission performed a flyby of Venus using a sail of almost 200 m^2 [7]. NASA followed up with a second demonstration mission in 2010, called Nanosail-D. This sail was significantly smaller, having a surface area of approximately 10 m^2 and was in a low Earth orbit [8]. The aim of this mission was to test the deployment of a sail to eventually be able to deorbit end-of-life spacecraft in future missions. After that, The Planetary Society's LightSail program has continued to launch photon sails into space. LightSail 1 was launched in 2015 and successfully deployed its solar sail. This first mission was to validate the deployment of a photon sail which layed a base for the second photon sail. LightSail 2 was launched in 2019 and demonstrated controlled photon sailing in low Earth orbit [9]. The deployed LightSail 2 is shown in Figure 1.1b. The most recently planned mission was the NEA Scout mission by NASA, which was launched at the end of 2022 and would have performed a flyby of a near-Earth asteroid. However, NASA was unable to make contact after the launch, after which NEA Scout was considered a failed mission[1].

As a future mission, the Breakthrough Starshot initiative announced plans to send small photon

[1] https://www.nasa.gov/centers/marshall/news/2022/nea-scout-status-update.html Retrieved on 22/06/2023

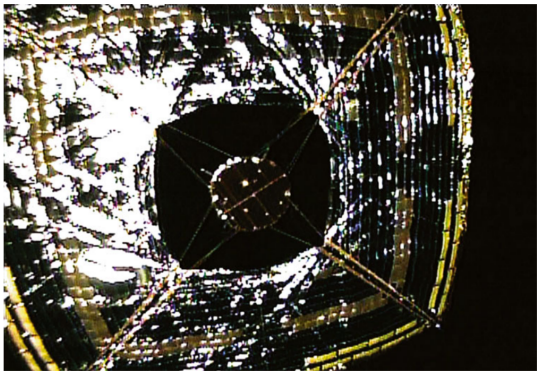

(a) IKAROS [10]

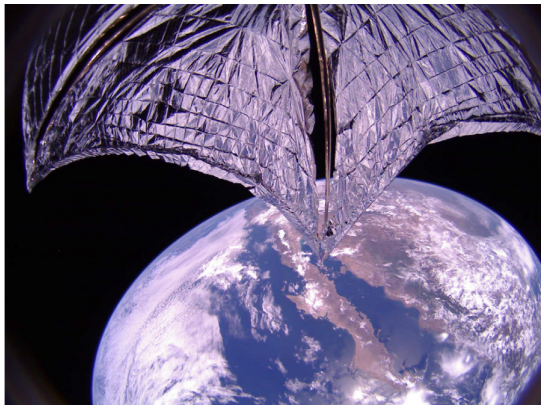

(b) LightSail 2 [9]

Figure 1.1: Deployed photon sails in space

Table 1.1: Radius, mass, luminosity and distance to the barycenter of the stars in the α-Cen system [1]

Star	Radius, $R_\odot$	Mass, $M_\odot$	Luminosity, $L_\odot$	Distance to barycenter, AU
α-Cen A	1.2234	1.1055	1.519	5.2 - 16.4
α-Cen B	0.8634	0.9373	0.5002	6.1 - 19.4
Proxima Centauri	0.1542	0.1221	0.0015	4300 - 13000

sails to the α-Centauri system, using a powerful laser array for propulsion[2]. This ambitious project has generated a large amount of interest and gave some new attention to the concept of photon sailing. Ongoing research on photon sailing focuses mainly on improving the materials of the sail, the deployment mechanisms, and navigation systems [8].

1.2. Alpha Centauri

The Alpha-Centauri (α-Cen) system has been observed for a long time as it is the third brightest star in the night sky [11]. The stellar system can be seen from the Southern Hemisphere in the Centauri constellation, as the stellar system has a declination of -60 deg. Until the 17th century, it was thought that the α-Cen system was a single star. The α-Cen system is the stellar system closest to Earth at a distance of 4.37 lightyears [11]. In 1689, while looking at a comet that passed in front of the α-Cen system, Jean Richaud observed that the star was actually a binary system consisting of the stars α-Cen A and B [12]. In 1915, a smaller star, α-Cen C or Proxima Centauri, which orbits the inner binary system, was observed by Robert Thorburn Innes [13]. Later, it was found that this smaller star was closer to the Sun than the other two stars in the system that were known before. This smaller star has an orbital period around the binary system of approximately 550,000 years [14]. Its current position and long orbital period imply that Proxima Centauri is the star closest to Earth since the first humans started investigating the stars. In the future, the star will move to the far-side of the binary system as viewed from Earth causing α-Cen A and B to be closer.

The α-Cen system consists of three stars, α-Cen A, B and C that all orbit the system's barycenter. α-Cen C is officially called Proxima Centauri. The mass, radius and luminosity of the three stars are shown in Table 1.1. In this table, all charachteristics of the stars are relative to the Sun, which is represented by $\odot$ as a subscript.

At the time of writing, three exoplanets have been observed around the smaller star Proxima Centauri. These planets are called Proxima b, c, and d [15],[16],[17]. Of these confirmed exoplanets, Proxima b is a terrestrial planet within the habitable zone of the star. The habitable zone is defined to be the region in a stellar system where liquid water could exist on an orbiting planet. Proxima c and d are not in the habitable zone. To date, no exoplanets have been discovered inside the binary system. The James Webb Space Telescope will search for planets around α-Cen A [18].

[2] `https://breakthroughinitiatives.org/initiative/3` Retrieved on 22/06/2023

The relatively close proximity and the fact that there are exoplanets in the system make it a very interesting stellar system to visit. In previous work, photon sailing was used to design a trajectory to the α-Cen system [19]. The previously mentioned Breakthrough Starshot also aims to design a mission to the system.

1.3. Previous work

Though mission scenarios towards the α-Cen system have been proposed, the photon-sailing dynamics within the α-Cen system has not yet been investigated extensively. References [19],[20] and [21] have investigated the dynamics of decelerating the photon sail in the α-Cen system after its interstellar journey. More research on the dynamics of and within the α-Cen system was conducted by investigating the artificial equilibrium points (AEPs). These AEPs have been investigated for the case of using a photon balloon [22] and a photon sail [1]. Next to that, trajectories within the α-Cen system were designed [23], [1] and [24]. The inner binary system in the α-Cen system is modeled in these papers as a three-body problem, with a spacecraft as the third body. In other three-body problems, like the Sun-Earth and Earth-Moon systems, motion around the (artificial) equilibrium points has been investigated extensively [25], [26] and [27]. Such periodic motion has been used in missions to study heliophysics and astrodynamics [28], [29]. Investigations into such motions in the α-Cen system are lacking in the literature. Eventually, missions towards the equilibrium points in the α-Cen system can be very insightful for heliophysical and astrodynamical studies because of the existence of two stars in the inner binary system. Therefore, the motion around the equilibrium points should be investigated first.

A multiple shooting differential correction (MSDC) algorithm is often used to find periodic orbits. This method has been used in the circular restricted three-body problem (CR3BP) [25], in the photon sail augmented CR3BP [30] and in the ER3BP [31]. Trajectories between the periodic orbits can be used to investigate the binary system further and observe it from different viewing points. Such heteroclinic-like trajectories within the α-Cen system have been investigated before using a genetic algorithm [1].

1.4. Research objective

Due to the relative proximity and the precense of exoplanets, the α-Cen system is a very interesting destination of the first interstellar travel with the use of photon pressure acceleration. As a basis to a future mission, the dynamics within the system need to be investigated first. Therefore, the research objective of this work is:

```
To design periodic orbits around the colinear Lagrange points
  in the Alpha Centauri system and design heteroclinic-like
       trajectories to connect these periodic orbits.
```

To be able to fulfill the research objective, the following research questions were made:

- What kind of planar Lyapunov orbits exist around the colinear Lagrange points in the α-Cen system using photon-pressure acceleration?
  - How do these Lyapunov orbits change when varying the lightness number of the photon-sail?
  - What is the effect of the initial true anomaly on these Lyapunov orbits?
- Is it possible to travel between the designed Lyapunov orbits in the α-Cen system using photon-pressure acceleration?

1.5. Report outline

The research is presented in the form of a journal article in Chapter 2. This journal article is written in the style of the American Institue of Aeronautics and Astronautics (AIAA). The article starts with an abstract and an introduction to the article. Then, a brief overview of the α-Cen system is given. A dynamics model that suits this system is presented after that and in the following section, the method and results of designing periodic orbits around the colinear Lagrange points are given. After that, the

method and results of the heteroclinic-like trajectories between the designed periodic orbits are given. Lastly, the article ends with the conclusions. In Chapter 3, more elaborate conclusions to the research are given. The answers to the research questions are presented here. Next to that, recommendations for future research are given here as well. The verification and validation of the used model is presented in Appendix A. Lastly, the plots with all the planar Lyapunov orbits for their β_{max} and its corresponding V_{max} are shown in Appendix B.

2

Journal Article

Photon-sail periodic orbits around the Lagrange points of the Alpha-Centauri system

Luc C.J. Haagh
Delft University of Technology, 2629 HS, Delft, The Netherlands

The first mission proposals to visit the Alpha Centauri system use photon-sail acceleration as a mode of propulsion to reach this stellar system closest to our own Solar System. To prepare for a future mission, the photon-sail dynamics in the system is investigated. Planar Lyapunov orbits around the colinear classical Lagrange points are designed to explore the Alpha Centauri system. This has been done before in other systems like the Earth-moon and Sun-Earth systems, but not yet in an elliptical binary star system. Starting with an initial guess in the circular restricted three-body problem without photon-sail acceleration, a Multiple Shooting Differential Correction (MSDC) algorithm changes the trajectory to a periodic orbit. A family of planar Lyapunov orbits is designed with increasing periods. Due to the eccentricity, the period of a Lyapunov orbit should be equal to the rotational period of the stellar system. The periodic orbits that satisfy this constraint are used to slowly increase the eccentricity of the model until it reaches a value of e = 0.5208, which is the eccentricity of the inner Alpha Centauri system. After that, the lightness number of the photon sail is increased to add photon-sail acceleration to the model up to a defined maximum of β_{max} = 2. A set of five constant steering laws is chosen to investigate its effect. Next to that, the moment at which the periodic orbit starts in terms of the true anomaly is varied as well. This results in a set of 40 families of periodic orbits with increasing lightness numbers. Depending on the orientation, the augmented Lyapunov orbit either shrinks into smaller orbits or expands into larger orbits when increasing the lightness number. If the orbit shrinks, it can either converge into an artificial equilibrium point or the photon-radiation pressure on the sail can become minimal. In that case, the Lyapunov orbit becomes (almost) independent of the lightness number and reaches β_{max} = 2. If the orbit expands, the maximum velocity will eventually go to infinity. At this vertical asymptote, the maximum lightness number is found. The initial true anomaly of Alpha Centauri θ_0 has a great effect on the Lyapunov orbits around L_2 and L_3 in the classical ER3BP. For θ_0 = 0, the orbit either converges to an AEP or the maximum velocity goes to infinity. For $\theta_0 = \pi$, a few orientations can reach β_{max} = 2. To further explore Alpha Centauri, an adaptive differential evolution algorithm is used to design trajectories between the Lyapunov orbits. The perfor-

mance of the algorithm is expressed as the Euclidean difference between the states at the end of the departure leg and the beginning of the arrival leg. Three different lightness numbers of 0.1, 0.5 and 2 are used for these trajectories. With a lightness number of 0.1, the dimensionless Euclidean error is in the range of 1E-1 to 1E-3, depending on the Lyapunov orbits. With this lightness number, the stars are also used as a gravity assist. For larger lightness numbers, the Euclidean error becomes negligible in the range 1E-7. With a lightness number of 2, the time of flight during the trajectory is significantly shorter. In future research, this can be further reduced using an MSDC algorithm.

Nomenclature

Roman

$\hat{\mathbf{n}}$	Normal vector of the photon sail
$\mathcal{A}(\hat{\mathbf{r}_A}, \hat{\boldsymbol{\theta}_A}, \hat{\boldsymbol{\phi}_A})$	Reference frame centred at photon sail with respect to α-Cen A
$\mathcal{B}(\hat{\mathbf{r}_B}, \hat{\boldsymbol{\theta}_B}, \hat{\boldsymbol{\phi}_B})$	Reference frame centred at photon sail with respect to α-Cen B
$O_{\mathcal{A}}(\hat{\mathbf{x}}_{O_{\mathcal{A}}}, \hat{\mathbf{y}}_{O_{\mathcal{A}}}, \hat{\mathbf{z}}_{O_{\mathcal{A}}})$	Observer reference frame centred at α-Cen A
$O_{\mathcal{B}}(\hat{\mathbf{x}}_{O_{\mathcal{B}}}, \hat{\mathbf{y}}_{O_{\mathcal{B}}}, \hat{\mathbf{z}}_{O_{\mathcal{B}}})$	Observer reference frame centred at α-Cen B
$\mathcal{S}_{\mathcal{P}}(\hat{\mathbf{x}}_{\mathcal{S}_{\mathcal{P}}}, \hat{\mathbf{y}}_{\mathcal{S}_{\mathcal{P}}}, \hat{\mathbf{z}}_{\mathcal{S}_{\mathcal{P}}})$	Pulsating synodic reference frame
$\mathbf{a}_s$	Photon-sail acceleration vector
$\mathbf{r}$	Position vector
$\mathbf{u}$	Child vector
$\mathbf{v}$	Velocity vector
$\mathbf{V}_1, \mathbf{V}_2, \mathbf{V}_3$	Parent vectors
$\mathbf{X}$	State vector
a	Semi-major axis
C	Constraints
CR	Crossover probability
e	Eccentricity
F	Scaling factor
i	Inclination
L	Luminosity
L_1, L_2, L_3	Colinear Lagrange points
M	Mass
N_{par}	Number of parameters
N_{pop}	Population size
R	Radius
T	Orbital period
T_1	Period of a single revolution
U	Effective potential

Greek

α	Cone angle
β	Lightness number
δ	Clock angle

ϵ	Conversion parameter for lightness number in other star systems
μ	Dimensionless mass of α-Cen B
Ω	Longitude of ascending node
ω	Argument of periapsis
Φ	State transition matrix
θ	True anomaly

Abbreviations

α-Cen	Alpha-Centauri
AU	Astronomical Unit
CR3BP	Circular Restricted three-body problem
EoM	Equations of Motion
ER3BP	Elliptical Restricted three-body problem
JADE	Adaptive differential evolution
MSDC	Multiple Shooting Differential Correction
PRP	Photon-radiation pressure
STM	State transition matrix
TOF	Time of flight
DE	Differential evolution

Subscripts

$\odot$	Sun
max	Maximum
x	Derivative with respect to x
y	Derivative with respect to y
A	Alpha-Centauri A
A	Arrival leg
B	Alpha-Centauri B
D	Departure leg

I. Introduction

Humanity has been fascinated by interstellar travel for a long time. The urge to explore more and more of humanity's surroundings is the driving motivation to visit another stellar system. Exploring other stellar systems also has a significant scientific relevance, because it enables humanity to gather more knowledge of our Solar System and the formation of stellar systems in general. The Alpha-Centauri (α-Cen) system is the stellar system closest to our Solar System and is therefore often considered to be the first destination of interstellar travel [1]. After the discovery of a rocky exoplanet in the habitable zone of the system in 2016, interest to visit the system has increased even more [2]. However, travelling to the α-Cen system would take approximately 75,000 years when using conventional spacecraft propulsion [3].

The use of photon-sail propulsion could drastically decrease the flight time for interstellar travel, although it uses tiny photon-radiation pressure as its sole source of propulsion [4]. Photon sailing is a proven concept as a means of propulsion in space. This has been demonstrated by missions like the IKAROS sail by JAXA, NASA's NanoSail-D2

and LightSail-1 and LightSail-2 by The Planetary Society [5], [6] and [7]. The improvement of photon-sail technology can eventually lead to the possibility of interstellar travel towards the α-Cen system. When using futuristic designs of photon sails, α-Cen can be reached in less than 80 years [3]. Possible missions with the goal of reaching places outside our Solar system have been investigated before [8] and the Breakthrough Starshot Project is an example of a proposed interstellar travel mission with the aim of reaching α-Cen $*$.

Although mission scenarios have been proposed, the photon-sailing dynamics within the α-Cen system has not yet been fully investigated. References [3],[9] and [10] have investigated the dynamics of decelerating the photon sail in α-Cen after its interstellar journey. The dynamics of artificial equilibrium points has been investigated using a photon balloon [11] and a photon sail [12]. Trajectories within the α-Cen system using photon-sail acceleration have been investigated as well. Examples of such trajectories are polar orbits about α-Cen A and B [13], heteroclinic-like motion between artificial equilibrium points [12] and a trajectory from α-Cen A and B towards Proxima Centauri [14]. The photon-sail augmented α-Cen system presents a three-body problem. In other three-body problems, like the Sun-Earth and Earth-Moon systems, motion around the equilibrium points has been investigated extensively [15], [16] and [17]. Such periodic motion has been used in missions to study heliophysics and astrodynamics [18], [19]. Investigations on such motions in α-Cen are lacking in the literature. Eventually, missions towards the equilibrium points in the α-Cen system can be very insightful for heliophysical and astrodynamical studies because of the existence of two stars in the inner binary system. Therefore, the motion around the equilibrium should first be investigated.

A multiple shooting differential correction (MSDC) algorithm is used to find periodic orbits in the photon-sail elliptical restricted three-body problem (ER3BP). This method has been used before to find periodic orbits in the circular restricted three-body problem (CR3BP) [15], in the photon-sail CR3BP [20] and in the ER3BP [21]. This MSDC is also used to design trajectories between periodic orbits. Such trajectories can be used to further investigate the binary system and observe it from different viewing points. These heteroclinic-like trajectories within the α-Cen system have been investigated before using a genetic algorithm [12], which often results in a trajectory that is not fully continuous. In this work, the MSDC is used to further decrease the discontinuity in the photon-sail trajectories. This method has been used in several Sun-planet systems [22], [23], [24], but again not under the effect of gravity and photon emission of two stars.

The α-Cen system is elaborated on in Chapter II and the dynamics model used in this research is discussed in Chapter III. The method and results of finding periodic orbits around the equilibrium points are shown in Chapter IV. The same is done for the method and results of designing a trajectory between the periodic orbits in Chapter V.

$*$`https://breakthroughinitiatives.org/initiative/3` Retrieved on 29/03/2023

II. Alpha Centauri

The α-Cen system consists of three stars, α-Cen A, B, and C, which all orbit the system's barycenter. α-Cen C is officially called Proxima Centauri and will be referred to as such in this paper. The mass, radius, luminosity and distance to the barycenter of each star are provided in Table 1. In this table, all values are relative to those of the Sun, which is represented by the subscript $\odot$.

Table 1 Radius, mass, luminosity and distance to the barycenter of the stars in the α-Cen system [12]

Star	Radius, $R_\odot$	Mass, $M_\odot$	Luminosity, $L_\odot$	Distance to barycenter, AU
α-Cen A	1.2234	1.1055	1.519	5.2 - 16.4
α-Cen B	0.8634	0.9373	0.5002	6.1 - 19.4
Proxima Centauri	0.1542	0.1221	0.0015	4300 - 13000

Stars α-Cen A and B form a binary system orbiting their barycenter, which is visually represented in Figure 1. In Figure 1a, the orbit is represented in the observer reference frames $\mathcal{O}_{\mathcal{A}}(\hat{\mathbf{x}}_{\mathcal{O}_{\mathcal{A}}}, \hat{\mathbf{y}}_{\mathcal{O}_{\mathcal{A}}}, \hat{\mathbf{z}}_{\mathcal{O}_{\mathcal{A}}})$. Frame $\mathcal{O}_{\mathcal{A}}$ is centred at α-Cen A and $\hat{\mathbf{z}}_{\mathcal{O}_{\mathcal{A}}}$ points to Earth, which means that the plane perpendicular to $\hat{\mathbf{z}}_{\mathcal{O}_{\mathcal{A}}}$ is the "plane of the sky" in Figure 1b. On this plane, $\hat{\mathbf{x}}_{\mathcal{O}_{\mathcal{A}}}$ points North and $\hat{\mathbf{y}}_{\mathcal{O}_{\mathcal{A}}}$ completes the right-handed reference frame. In Figure 1b, the "plane of the sky" is the plane perpendicular to the zenith of the Earth. The apparent orbits are projected on the plane of the sky, which are the orbits as we observe them from Earth. Both α-Cen A and B orbit their common barycenter with a period of 79.9 years [12] and an eccentricity of 0.5208. The inclination is defined as the angle between the orbital plane and the 'plane of the sky' and has a value of 79.320 deg. All Keplerian elements of α-Cen B in $\mathcal{O}_{\mathcal{A}}$ are shown in Table 2. Here, the longitude of the ascending node is measured east of the vector $\hat{\mathbf{x}}_{\mathcal{O}_{\mathcal{A}}}$. Figure 1b shows a three-dimensional visualisation of the orbits in frame $\mathcal{O}_{\mathcal{B}}$, which is similar to frame $\mathcal{O}_{\mathcal{A}}$, but the centre is shifted to the barycenter of the system.

Table 2 Keplerian elements of α-Cen B in reference frame $\mathcal{O}_{\mathcal{A}}$ [12]

Parameter	Unit	Value
Semi-major axis a	AU	23.517
Eccentricity e	-	0.5208
Inclination i	deg	79.320
Longitude of ascending node Ω	deg	205.064
Argument of periapsis ω	deg	232.006
Orbital period T	yr	79.929

III. Dynamics model

To model the motion of a photon sail within α-Cen, the dynamical framework of the ER3BP is used due to the high eccentricity of the inner binary system. An additional term for the Photon-radiation pressure (PRP) force is added in

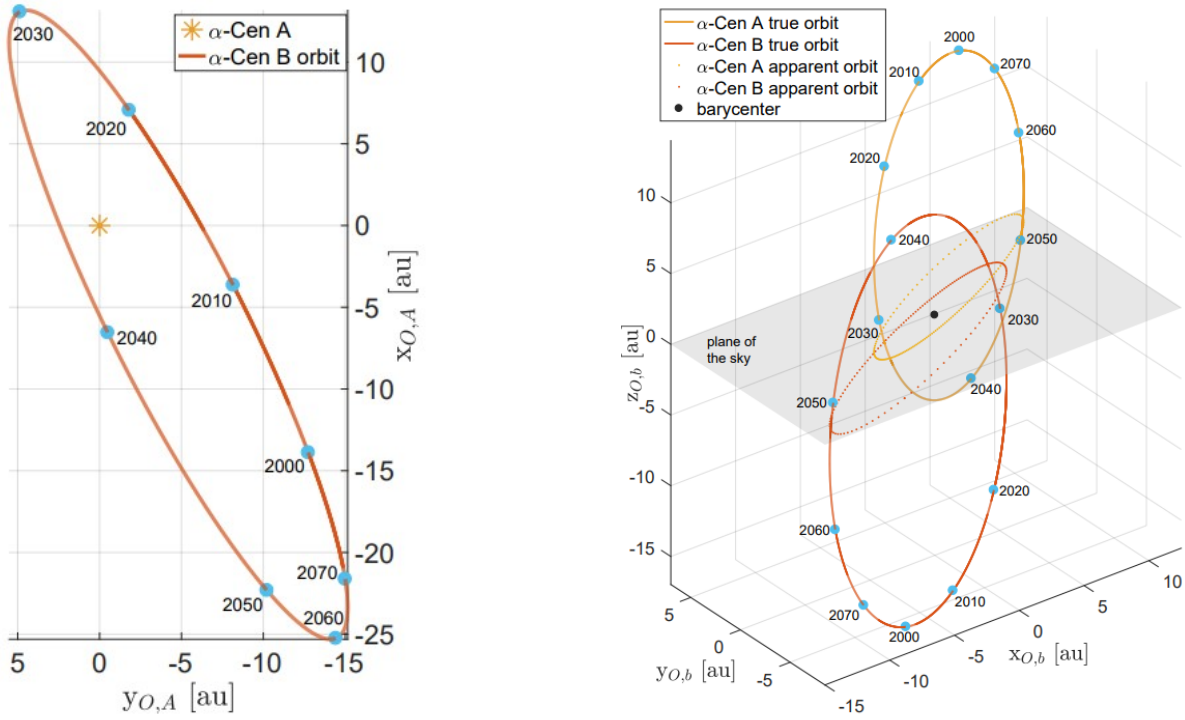

(a) **(b)**

Fig. 1 Orbits of α-Cen AB system in a) $O_{\mathcal{A}}$ and b) $O_{\mathcal{B}}$ [12]

the equations of motion (EoMs). This results in the PRP-augmented ER3BP.

A. Photon-Radiation Pressure augmented Elliptical Restricted Three-Body Problem

In the ER3BP, the two primary bodies α-Cen A and B have an elliptical orbit around their common barycenter. It is assumed that the third body, the photon sail, has a negligible mass and that its motion is only affected by the gravitational acceleration of the two primaries and the PRP acceleration, because the two primaries are photon-emitting sources. To describe the EoM in the elliptical restricted three-body problem, a pulsating synodic reference frame is used. The pulsating synodic reference frame $\mathcal{S}_{\mathcal{P}}(\hat{\mathbf{x}}_{\mathcal{S},\mathcal{P}}, \hat{\mathbf{y}}_{\mathcal{S},\mathcal{P}}, \hat{\mathbf{z}}_{\mathcal{S},\mathcal{P}})$ places the centre of the reference frame at the barycenter between the two primary bodies. The $\hat{\mathbf{x}}_{\mathcal{S},\mathcal{P}}$-axis is defined in such a way that both α-Cen A and B are located on this axis with the positive direction toward α-Cen B. The $\hat{\mathbf{z}}_{\mathcal{S},\mathcal{P}}$-axis is in the direction of the angular momentum vector of the binary system, and the $\hat{\mathbf{y}}_{\mathcal{S},\mathcal{P}}$-axis completes the right-handed reference frame. As an observer in an inertial frame looking towards the reference frame centre from the positive $\hat{\mathbf{z}}_{\mathcal{S},\mathcal{P}}$-direction, the reference frame is rotating. Due to the eccentricity of the orbits of the stars, this rotation is non-uniform. Due to the pulsating frame, the stars are fixed along the $\hat{\mathbf{x}}_{\mathcal{S},\mathcal{P}}$-axis even though the distance of the stars to the barycenter varies depending on the true anomaly (θ) of the system, because of the eccentricity of the system. For that reason, the non-uniform rotating, pulsating synodic

reference frame $\mathcal{S}_P$ is used. Frame $\mathcal{S}_P$ pulsates, which means that in addition to a rotation, it contracts and expands in such a way that both stars are stationary on the $\hat{\mathbf{x}}$-axis. A visual representation of this reference frame is shown in Figure 2, where the non-uniform rotational velocity is represented with the vector $\boldsymbol{\omega}$. The vector from α-Cen A or B towards the spacecraft is denoted using $\mathbf{r}_A$ and $\mathbf{r}_B$, respectively.

In frame $\mathcal{S}_\mathcal{P}$, the EoMs are defined as [25]:

$$x'' - 2y' = \frac{1}{1 + e\cos\theta}\left(\frac{\delta U}{\delta x} + \mathbf{a}_{s,x}\right) \tag{1}$$

$$y'' + 2x' = \frac{1}{1 + e\cos\theta}\left(\frac{\delta U}{\delta y} + \mathbf{a}_{s,y}\right) \tag{2}$$

$$z'' + z' = \frac{1}{1 + e\cos\theta}\left(\frac{\delta U}{\delta z} + \mathbf{a}_{s,z}\right) \tag{3}$$

Here, the differentiation on the left-hand side occurs with respect to the true anomaly of the system. The photon-sail acceleration vector is denoted using $\mathbf{a}_s$ and will be defined later. The effective potential combines the gravitational and centripetal potentials and is denoted as U. This effective potential is defined as:

$$U = \frac{1}{2}(x^2 + y^2 + z^2) + \frac{1-\mu}{||\mathbf{r}_A||} + \frac{\mu}{||\mathbf{r}_B||} \tag{4}$$

The equations of motions are dimensionless in terms of mass, distance and time. The unit of mass is the sum of the mass of α-Cen A and B. The unit of distance is defined as the instantaneous distance between α-Cen A and B, and the unit of time is defined as the inverse of the mean motion of the two stars. Therefore, the dimensionless orbital period becomes 2π. The dimensionless mass of α-Cen B, μ is introduced using:

$$\mu = \frac{M_B}{M_A + M_B} \tag{5}$$

Table 1 provided the masses of α-Cen A and B as 1.1055 and 0.9373 times the mass of the Sun, respectively. Using Eq. 5 this results in a dimensionless mass of α-Cen B of μ = 0.4588. In reference frame $\mathcal{S}_\mathcal{P}$, α-Cen A is located at [$-\mu$,0,0] and α-Cen B is located at [1-μ,0,0], which can be seen in Figure 2.

B. Photon-Radiation Pressure Acceleration

The photon-sail accelerations are part of the EoMs of the spacecraft in Eqs. 1 - 3. In our own Solar System, the Sun is the main photon-emitting source. In the α-Cen system, both α-Cen A and B emit photons that accelerate the spacecraft. For that reason, the photon acceleration term ($\mathbf{a}_s$) is the sum of the acceleration from α-Cen A ($\mathbf{a}_{s,A}$) and α-Cen B ($\mathbf{a}_{s,B}$). To determine the PRP acceleration caused by the photon pressure, an ideal sail is assumed. An ideal photon

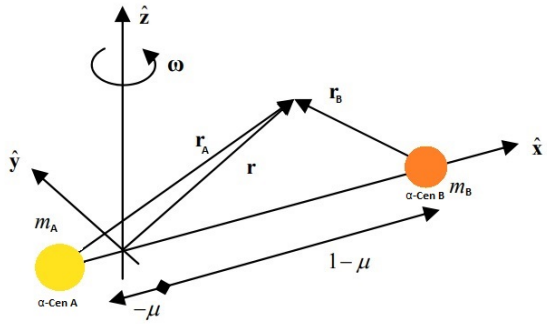

Fig. 2 Schematic of the α-Cen A/B elliptical restricted three-body problem and reference frame $\mathcal{S}_{\mathcal{P}}(\hat{\mathbf{x}}, \hat{\mathbf{y}}, \hat{\mathbf{z}})$ (not to scale)

sail reflects all incoming photons and does not absorb any photons. In addition, it is assumed that there is pure specular reflection of the photons, which means that the angle of reflection is the same as the angle of incidence. Therefore, the acceleration vector is parallel to the normal vector ($\hat{\mathbf{n}}$) of the photon sail [4]. The direction of $\hat{\mathbf{n}}$ is defined using the cone angle and the clock angle α and δ, respectively. These angles are defined within the frames $\mathcal{A}(\hat{\mathbf{r}}_A, \hat{\boldsymbol{\theta}}_A, \hat{\boldsymbol{\phi}}_A)$ and $\mathcal{B}(\hat{\mathbf{r}}_B, \hat{\boldsymbol{\theta}}_B, \hat{\boldsymbol{\phi}}_B)$, which are shown in Figure 3. Here, $\hat{\boldsymbol{\phi}}_A$ and $\hat{\boldsymbol{\phi}}_B$ are defined as being in the $\hat{\mathbf{z}}$-direction. Then, $\hat{\boldsymbol{\theta}}_A$ and $\hat{\boldsymbol{\theta}}_B$ complete the right-handed reference frames. In Figure 3b, the subscript i stands for A or B.

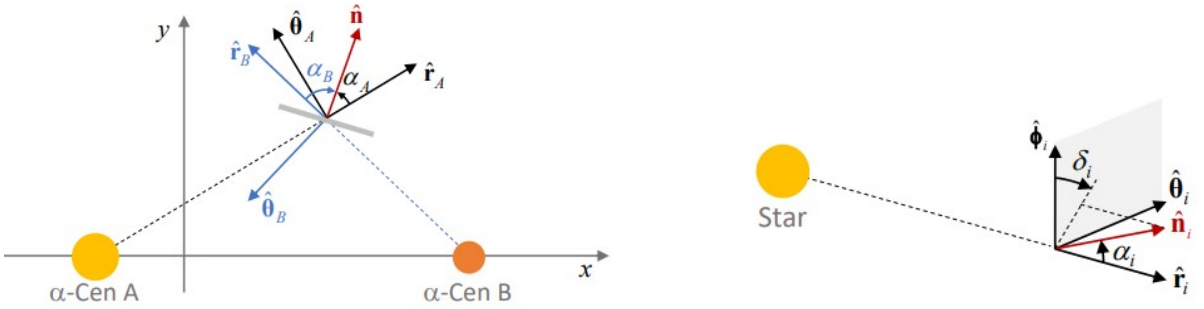

(a) Reference frames $\mathcal{S}_{\mathcal{P}}$, $\mathcal{A}$ and $\mathcal{B}$ **(b) Definition of cone- and clock angles (α and δ)**

Fig. 3 Photon sail orientation [12]

In both reference frames $\mathcal{A}$ and $\mathcal{B}$, the normal vector $\hat{\mathbf{n}}_i$ is defined as:

$$\hat{\mathbf{n}}_i = \begin{bmatrix} \cos(\alpha_i) & \sin(\alpha_i)\sin(\delta_i) & \sin(\alpha_i)\cos(\delta_i) \end{bmatrix}^T, \quad i = A, B \tag{6}$$

To determine the orientation of the normal vector of the photon sail in frame $\mathcal{S}_{\mathcal{P}}$, a reference frame transformation is performed from frames $\mathcal{A}$ and $\mathcal{B}$ to $\mathcal{S}_{\mathcal{P}}$ using:

$$\hat{\mathbf{n}}_{\mathcal{S}_{\mathcal{P}}} = \begin{bmatrix} \hat{\mathbf{r}}_i & \hat{\boldsymbol{\theta}}_i & \hat{\boldsymbol{\phi}}_i \end{bmatrix} \hat{\mathbf{n}}_i, \quad i = A, B \tag{7}$$

From now on, the normal vectors $\hat{\mathbf{n}}$ are given in the $\mathcal{S}_{\mathcal{P}}$ frame, as the PRP acceleration will also be defined in this frame. For two emitting sources, the PRP acceleration vector is given as [12]:

$$\mathbf{a}_s = \mathbf{a}_{s,A} + \mathbf{a}_{s,B} = \beta_A \frac{1-\mu}{||\mathbf{r}_A||^2}(\hat{\mathbf{r}}_A \cdot \hat{\mathbf{n}})^2 \hat{\mathbf{n}} \; + \; \beta_B \frac{\mu}{||\mathbf{r}_B||^2}(\hat{\mathbf{r}}_B \cdot \hat{\mathbf{n}})^2 \hat{\mathbf{n}} \tag{8}$$

Here, the lightness number β is a parameter to indicate the performance of the photon sail in terms of the acceleration it can produce. It is defined as the ratio of the PRP acceleration to the gravitational acceleration and, therefore, depends on the characteristics of the photon sail and the star(s) it orbits [4]. For that reason, a separate lightness number is introduced for α-Cen A and B. If a star has a larger mass than our Sun, the gravitational acceleration will be larger, which would decrease the lightness number of the sail with respect to a sail in proximity of the Sun. On the other hand, a higher luminosity of the star increases the photon-pressure acceleration, which increases the lightness number. The relation between the lightness number around the Sun ($\odot$) compared to that around other stars is given by [3]:

$$\beta_i = \beta_\odot \frac{L_i M_\odot}{L_\odot M_i} = \epsilon_i \beta_\odot, \quad i = A, B \tag{9}$$

One of the first photon sails in space, IKAROS, had a lightness number with respect to the Sun of $\beta_\odot = 0.001$ [26]. More modern photon sails, such as that of the NEA Scout, are reaching values in the order of $\beta_\odot = 0.01$ [27]. This shows that the performance of photon sails is improving rapidly. In the future, the lightness number is expected to increase to a range between 0.025 and 0.04 [28]. Using more futuristic photon sails with new materials such as graphene, the lightness number can increase massively, up to $\beta_\odot = 1779$ [3].

Current photon sails also absorb part of the incoming photons, which increases the temperature of the sail. As a means of thermal control, only one side has a reflective side and the other side is used for thermal emission. Therefore, only the reflective side can be pointed towards the photon source, which means that the normal vectors $\hat{\mathbf{n}}_A$ and $\hat{\mathbf{n}}_B$ ideally need to align. However, future photon sails are expected to have a reflective coating on both sides. As travelling to α-Cen is considered a futuristic mission, it is assumed that a two-sided reflective sail is available at that time. Therefore, only two-sided sails are considered in this research. This means that both $\hat{\mathbf{n}}_A = \hat{\mathbf{n}}_B$ and $\hat{\mathbf{n}}_A = -\hat{\mathbf{n}}_A$ are possible.

IV. Periodic Orbits

Periodic orbits around the classical Lagrange points in the α-Cen system are designed using a MSDC algorithm. In this paper, only planar Lyapunov orbits around the colinear Lagrange points are designed. The triangular Lagrange points in systems where the secondary body has a small mass are stable, making them scientifically interesting, as natural bodies can stay at this Lagrange point. However, for systems where the mass of the secondary body is larger than the Gascheau's value, so $\mu > 0.0385$, the triangular Lagrange points are not stable, which is the case for α-Cen [29]. As there are no natural objects expected at the triangular Lagrange points, this paper solely focuses on planar Lyapunov

orbits around the colinear Lagrange points. As these orbits stay on the xy-plane, the defined three-dimensional dynamics model in Section III is reduced to a two-dimensional model.

A. Methodology

The MSDC algorithm is an iterative process at two levels, which is visualised in Figure 4. An initial guess is improved to a continuous trajectory in terms of position in Figure 4a. This first level is described in Subsection IV.A.1. The approach of the second level is shown in Figure 4b, where the trajectory is made continuous in both position and velocity. This process is described in Subsection IV.A.2. The method used in this section has been described by Howell and Pernicka [17].

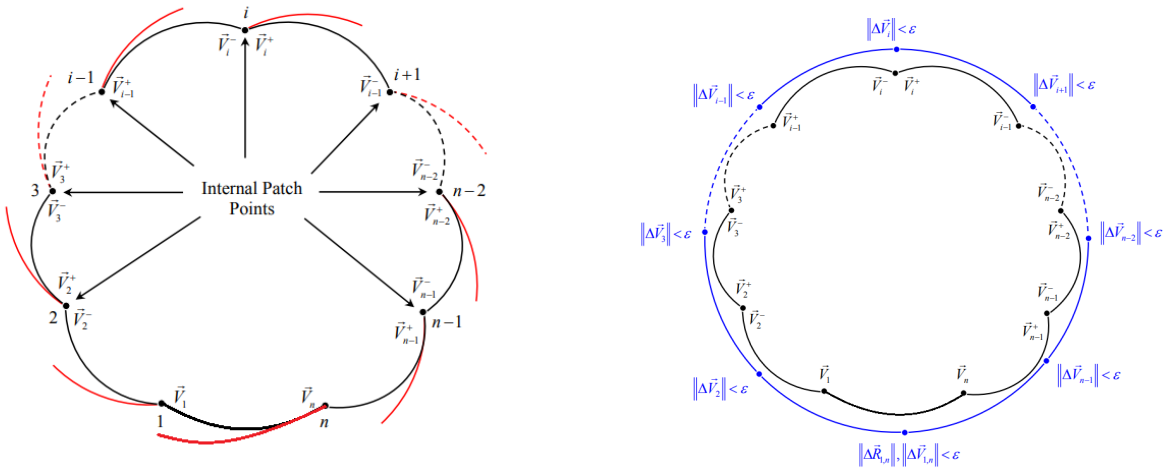

(a) Level 1: Design continuous trajectory in terms of position (Subsection IV.A.1)

(b) Level 2: Design continuous trajectory in terms of position and velocity (Subsection IV.A.2)

Fig. 4 Two-level iterative process of multiple shooting differential correction [15]

The algorithm finds a solution by linearising the EoM to $\dot{\mathbf{X}} = A\mathbf{X}$. Here, the state vector $\mathbf{X} \in \mathbb{R}^4$ belongs to the two-dimensional phase space and is therefore the column vector; $[x, y, \dot{x}, \dot{y}]^T$. From literature [12], the matrix $A(\theta)$ in the PRP-augmented ER3BP model is defined as

$$A(\theta) = \begin{bmatrix} 0 & I \\ \frac{K}{1+e\cos(\theta)} & S \end{bmatrix}, \quad \text{with} \quad K = \begin{bmatrix} U_{xx} + \frac{\delta a_{s,x}}{\delta x} & U_{xy} + \frac{\delta a_{s,x}}{\delta y} \\ U_{yx} + \frac{\delta a_{s,y}}{\delta x} & U_{yy} + \frac{\delta a_{s,y}}{\delta y} \end{bmatrix}, \quad I = \begin{bmatrix} 1 & 0 \\ 0 & 1 \end{bmatrix}, \quad S = \begin{bmatrix} 0 & 2 \\ -2 & 0 \end{bmatrix} \tag{10}$$

The first step of the algorithm is to make an initial guess of the periodic orbit around a Lagrange point. This is done by perturbing a spacecraft at the Lagrange point along the eigenvector which is associated to the imaginary eigenvalue of matrix A(θ). These eigenvectors correspond to stable motion around the Lagrange point. The size of the perturbation

is set to 0.01 in dimensionless units. After applying the perturbation, the new state is propagated forward until it passes the $\hat{\mathbf{x}}$-axis in the same direction as it started. The trajectory is divided in N segments, where each segment starts at a separate patch point. In Figure 5, the initial guess for a periodic orbit around the L_1 point is shown.

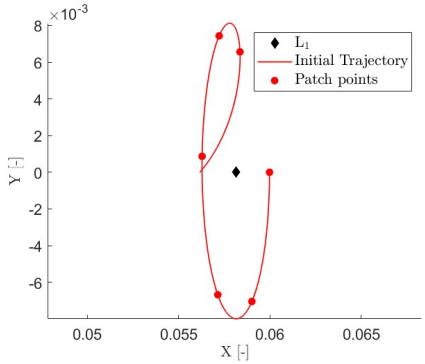

Fig. 5 Initial guess for a periodic orbit around L_1

Here, the trajectory is not continuous in both position and velocity as the last segment of the trajectory does not arrive at the first patch point. Therefore, the first level of the MSDC algorithm is used to make the trajectory continuous in position first.

1. Continuous trajectory in position

The first step is to make the trajectory a continuous path of multiple segments in terms of position. The MSDC uses the State Transition Matrix (STM), denoted as $\Phi(\theta, \theta_0)$ to correct the state of each patch point ($\mathbf{X}_i$) in order to reach the next patch point ($\mathbf{X}_{i+1}$). As the aim is to find a periodic orbit, the last patch point is corrected in such a way that it reaches the first patch point. The initial STM ($\Phi(\theta_0, \theta_0)$) is an identity matrix I of size 4x4 and is propagated using the derivative of the STM which is calculated using $\frac{\delta\Phi}{\delta\theta}(\theta, \theta_0) = A(\theta)\Phi(\theta, \theta_0)$. Using the state $\mathbf{X}_i$, the trajectory and STM are numerically propagated. After this propagation, there is a difference between the position at the end of the propagated trajectory ($\mathbf{r}_f$) and the position of the next patch point ($\mathbf{r}_{i+1}$). The goal of the algorithm is to minimise this difference in position $\delta\mathbf{r}_f$. The difference in state $\delta\mathbf{X}_f$ can be linearly approximated using Eq. 11 [17]. Here, the subscript i stands for the patch point at the start of the segment. The subscript f belongs to the state at the end of the propagated trajectory and the subscript $i+1$ belongs to the state of the next patch point. The relation in Eq. 11 is used to correct the velocity of the patch point to minimise $\delta\mathbf{r}_f$. The last term in this equation is added to linearly approximate $\delta\mathbf{X}_f$ for a change in time of flight $\delta(\theta_f - \theta_i)$.

$$\delta \mathbf{X}_f = \begin{bmatrix} \delta x_f \\ \delta y_f \\ \delta \dot{x}_f \\ \delta \dot{y}_f \end{bmatrix} \cong \Phi(\theta_f, \theta_i) \begin{bmatrix} \delta x_i \\ \delta y_i \\ \delta \dot{x}_i \\ \delta \dot{y}_i \end{bmatrix} + \begin{bmatrix} \dot{x}_f \\ \dot{y}_f \\ \ddot{x}_f \\ \ddot{y}_f \end{bmatrix} \delta(\theta_f - \theta_i) \tag{11}$$

As the state vector $\mathbf{X}_f$ contains four different states and the goal is to minimize $\delta \mathbf{r}_f$, only the first two rows of the matrix equation are considered. Using these first two rows, the effect of changing the initial state on the final position is linearly approximated. It is assumed that the initial position is correct, and therefore they do not change. In these two rows, there are three remaining unkowns, $\delta \dot{x}_i$, $\dot{y}_i$ and $\delta(\theta_f - \theta_i)$. To solve these unknowns, Eq. 11 is rewritten in the linear form:

$$L\mathbf{u} = \mathbf{b} \tag{12}$$

Here, L, $\mathbf{u}$ and $\mathbf{b}$ are the matrices and vectors defined as

$$L = \begin{bmatrix} \Phi_{13} & \Phi_{14} & \dot{x} \\ \Phi_{23} & \Phi_{24} & \dot{y} \end{bmatrix}_f, \quad \mathbf{u} = \begin{bmatrix} \delta \dot{x}_i \\ \delta \dot{y}_i \\ \delta(\theta_f - \theta_i) \end{bmatrix} \text{ and } \mathbf{b} = \begin{bmatrix} \delta x_f \\ \delta y_f \end{bmatrix} = \delta \mathbf{r}_f \tag{13}$$

To make the trajectory continuous in position, the goal is to minimise $\delta \mathbf{r}_f$ in terms of the smallest Euclidean norm for Eq. 12, the following relation is used:

$$\mathbf{u} = L^T (L L^T)^{-1} \mathbf{b} \tag{14}$$

With this equation, the required change in initial velocity is approximated. By iterating this process until $\delta \mathbf{r}_f$ converges below a tolerance of $\epsilon < 10^{-9}$, a state for each patch point is found. Using the initial guess which was shown in Figure 5, the trajectory is made continuous in terms of position. This results in the trajectory shown in Figure 6. The trajectory is designed to be continuous in terms of position, but there is still a velocity difference $\delta \mathbf{v}$ between the segments, at each patch point.

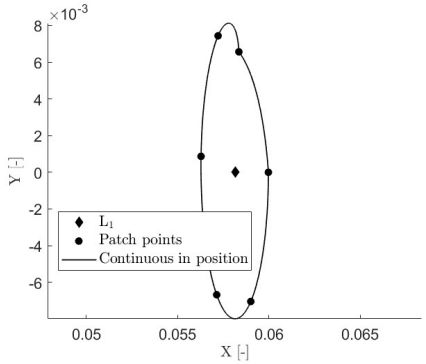

Fig. 6 Trajectory continuous in position using MSDC algorithm

2. Continuous trajectory in velocity

Next, the velocity difference between the segments $\delta\mathbf{v}$ are minimised by looking at two subsequent segments simultaneously. For example, the initial and final states of segment 1 are denoted using the subscriptions 'o' and 'p$^-$'. For segment 2, the patch points are denoted as 'p$^+$' and 'f' for the initial and final state. These denotations are visualised in Figure 7. The difference in velocity at the patch point p between the two segments is defined as $\delta\mathbf{v}_p = \mathbf{v}_{p^+} - \mathbf{v}_{p^-}$. Here, $\mathbf{v}_{p^+}$ is known by integrating backward from $\mathbf{X}_f$ toward $\mathbf{X}_{p^+}$ and $\mathbf{v}_{p^-}$ is known by integrating forward from $\mathbf{X}_0$ toward $\mathbf{X}_{p^-}$.

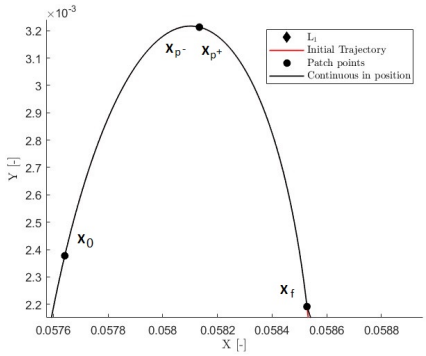

Fig. 7 Two subsequent segments which are continuous in position

To make the trajectory continuous in velocity, the positions of all three patchpoints $\mathbf{r}_o$, $\mathbf{r}_p$ and $\mathbf{r}_f$ are changed in such a way that the $\delta\mathbf{v}_p$ is minimised. using the following variation of Eq. 11 [17]

$$\delta\mathbf{X}_{p^+} = \begin{bmatrix} \delta x_{p^+} \\ \delta y_{p^+} \\ \delta \dot{x}_{p^+} \\ \delta \dot{y}_{p^+} \end{bmatrix} \cong \Phi(\theta_{p^+}, \theta_f) \begin{bmatrix} \delta x_f \\ \delta y_f \\ \delta \dot{x}_f \\ \delta \dot{y}_f \end{bmatrix} + \begin{bmatrix} \dot{x}_{p^+} \\ \dot{y}_{p^+} \\ \ddot{x}_{p^+} \\ \ddot{y}_{p^+} \end{bmatrix} \delta(\theta_{p^+} - \theta_f) \tag{15}$$

The STM is divided into four smaller matrices of size 2x2 as

$$\Phi(t_p, t_f) = \begin{bmatrix} A_{pf} & B_{pf} \\ C_{pf} & D_{pf} \end{bmatrix} \tag{16}$$

Using this notation for the STM and dividing the states into position, velocity and acceleration, Eq. 15 can be rewritten as

$$\begin{bmatrix} \delta\mathbf{r}_{p^+} \\ \delta\mathbf{v}_{p^+} \end{bmatrix} = \begin{bmatrix} A_{pf} & B_{pf} \\ C_{pf} & D_{pf} \end{bmatrix} \begin{bmatrix} \delta\mathbf{r}_f \\ \delta\mathbf{v}_f \end{bmatrix} + \begin{bmatrix} \mathbf{v}_{p^+} \\ \mathbf{a}_{p^+} \end{bmatrix} (\delta\theta_{p^+} - \delta\theta_f) \tag{17}$$

Then, the first vector equation is used to solve $\delta\mathbf{v}_f$

$$\delta\mathbf{v}_f = B_{pf}^{-1}\delta\mathbf{r}_{p^+} - B_{pf}^{-1}A_{pf}\delta\mathbf{r}_f - B_{pf}^{-1}\mathbf{v}_{p^+}(\delta\theta_{p^+} - \delta\theta_f) \tag{18}$$

This is then substituted into the second vector equation of Eq. 17 to find an equation for $\delta\mathbf{v}_{p^+}$

$$\delta\mathbf{v}_{p^+} = (C_{pf} - D_{pf}B_{pf}^{-1}A_{pf})\delta\mathbf{r}_f + D_{pf}B_{pf}^{-1}\delta\mathbf{r}_{p^+} - (D_{pf}B_{pf}^{-1}\mathbf{v}_{p^+} - \mathbf{a}_{p^+})(\delta\theta_{p^+} - \delta\theta_f) \tag{19}$$

The same method is used for the first segment which is propagated from patch point o to p^-. For this segment, the STM is also divided into four 2x2 matrices as follows

$$\Phi(t_p, t_o) = \begin{bmatrix} A_{po} & B_{po} \\ C_{po} & D_{po} \end{bmatrix} \tag{20}$$

The relation between $\delta\mathbf{v}_{p^-}$ and a change of the positions $\mathbf{r}_o$ and $\mathbf{r}_p$ is then as follows

$$\delta\mathbf{v}_{p^-} = (C_{po} - D_{po}B_{po}^{-1}A_{po})\delta\mathbf{r}_o + D_{po}B_{po}^{-1}\delta\mathbf{r}_{p^-} - (D_{po}B_{po}^{-1}\mathbf{v}_{p^-} - \mathbf{a}_{p^-})(\delta\theta_{p^-} - \delta\theta_o) \tag{21}$$

Subtracting $\delta\mathbf{v}_{p^+}$ and $\delta\mathbf{v}_{p^-}$ will result in a change in velocity discontinuity ($\delta\Delta\mathbf{v}_p$). As the goal of this method is to set the velocity discontinuity at patch point p to zero, the required change is set to the existing discontinuity by integrating backwards and forwards towards point p. Therefore, $\delta\Delta\mathbf{v}_p = -\Delta\mathbf{v}_p$. The subtraction of Eq. 21 from Eq. 19 results in

$$-\Delta \mathbf{v}_p = \begin{bmatrix} M_{\mathbf{r}_o} & M_{\theta_o} & M_{\mathbf{r}_p} & M_{\theta_p} & M_{\mathbf{r}_f} & M_{\theta_f} \end{bmatrix} \begin{bmatrix} \delta \mathbf{r}_o \\ \delta \theta_o \\ \delta \mathbf{r}_p \\ \delta \theta_p \\ \delta \mathbf{r}_f \\ \delta \theta_f \end{bmatrix} \tag{22}$$

Here, the six values in the M-matrix are described as

$$M_{\mathbf{r}_o} = D_{po} B_{po}^{-1} A_{po} - C_{po} \tag{23}$$

$$M_{t_o} = \mathbf{a}_{p^-} - D_{po} B_{po}^{-1} \mathbf{v}_{p^-} \tag{24}$$

$$M_{\mathbf{r}_p} = D_{pf} B_{pf}^{-1} - D_{po} B_{po}^{-1} \tag{25}$$

$$M_{t_p} = D_{po} B_{po}^{-1} \mathbf{v}_{p^-} - D_{pf} B_{pf}^{-1} \mathbf{v}_{p^+} + \mathbf{a}_{p^+} - \mathbf{a}_{p^-} \tag{26}$$

$$M_{\mathbf{r}_f} = C_{pf} - D_{pf} B_{pf}^{-1} A_{pf} \tag{27}$$

$$M_{t_f} = D_{pf} B_{pf}^{-1} \mathbf{v}_{p^+} - \mathbf{a}_{p^+} \tag{28}$$

In Eq. 22, there are six unknowns in two equations, being $\mathbf{r}_o$, θ_o, $\mathbf{r}_p$, θ_p, $\mathbf{r}_f$ and θ_f. Again, the smallest Euclidean norm of $\Delta \mathbf{v}_p$ should be found, as was done using Eq. 14. Therefore, a change of position and time at points 'o', 'p' and 'f' can be achieved by using

$$\begin{bmatrix} \delta \mathbf{r}_o \\ \delta t_o \\ \delta \mathbf{r}_p \\ \delta t_p \\ \delta \mathbf{r}_f \\ \delta t_f \end{bmatrix} = -[M^T (M M^T)^{-1} \Delta \mathbf{v}_p] \tag{29}$$

The location of the three points is then updated by $\mathbf{R}_{new} = \mathbf{R}_{old} + \delta \mathbf{r}$. Until now, the trajectory consisted of only two segments and was not periodic. Therefore, more segments are added and extra constraints are added to make the trajectory periodic and continuous in position and velocity.

3. Increase the number of segments and add extra constraints

To ensure a periodic orbit, multiple segments and additional constraints are added to the algorithm. The general form of Eq. 22, is shown in Eq. 30. Here, -$\Delta\mathbf{v}$ is the discontinuity at each patch point and C stands for the extra constraints that can be added to the problem. The additional segments causes the M-matrix to have more rows for each internal patch point. These extra rows are shown in Eq. 31, above the dashed line. Next to adding extra segments, additional constraints are needed to design a periodic orbit. A periodic orbit is designed once the end point of the last segment 'n' coincides with the start point of the first segment '0'. To maintain the periodic motion around the Lagrange point, the EoMs in Eqs. 1-3 should be periodical as well. In a CR3BP, the EoMs are solely depending on the position and velocity of a spacecraft, but in an ER3BP the EoMs are depending on the cosine of the true anomaly of the system as well. Therefore, the EoMs are periodical over a period of 2π, when keeping the state $\mathbf{X}$ constant. For that reason, points 'n' and '0' should be continuous in position and velocity and the total time of flight (TOF) to go from '0' to 'n' should be 2π, or a multiple or fraction of 2π. For example, if the period of one revolution (T_1) is π, two revolutions are needed for a periodical motion to occur. Therefore, the constraint $T_1 = \frac{2m\pi}{N}$, where m and N are integers is added to the MSDC. Adding these constraints to an MSDC has been done before [30]. A generalised form of Eq. 22 is

$$[M][\delta\mathbf{r}] = \begin{bmatrix} -\Delta\mathbf{v} \\ \hdashline C \end{bmatrix} \tag{30}$$

Here, C is a placeholder for any constraint that are added to the MSDC algorithm. When designing a periodic orbit, the three constraints are added to the MSDC for a trajectory with n segments. This results in the M-matrix, and vectors $\delta\mathbf{r}$ and $-\Delta\mathbf{v}$ where the constraints are under the dashed lines in the matrices, as follows

$$[\delta\mathbf{r}] = \begin{bmatrix} \delta\mathbf{r}_0 \\ \delta\theta_0 \\ \delta\mathbf{r}_1 \\ \delta\theta_1 \\ \delta\mathbf{r}_2 \\ \delta\theta_2 \\ \vdots \\ \delta\mathbf{r}_{n-1} \\ \delta\theta_{n-1} \end{bmatrix}, \quad \begin{bmatrix} -\Delta\mathbf{v} \\ \hdashline C \end{bmatrix} = \begin{bmatrix} -\Delta\mathbf{v}_1 \\ -\Delta\mathbf{v}_2 \\ -\Delta\mathbf{v}_3 \\ \vdots \\ -\Delta\mathbf{v}_{n-1} \\ \hdashline \vec{r}_n - \vec{r}_1 \\ \vec{v}_n - \vec{v}_1 \\ T_1 - (\theta_n - \theta_1) \end{bmatrix} \tag{31}$$

$$
[M] = \left[\begin{array}{cccccccccc}
M_{\mathbf{r}_{o_1}} & M_{t_{o_1}} & M_{\mathbf{r}_{p_1}} & M_{t_{p_1}} & M_{\mathbf{r}_{f_1}} & M_{t_{f_1}} & 0 & 0 & \dots & 0 \\
0 & 0 & M_{\mathbf{r}_{o_2}} & M_{t_{o_2}} & M_{\mathbf{r}_{p_2}} & M_{t_{p_2}} & M_{\mathbf{r}_{f_2}} & M_{t_{f_2}} & \dots & 0 \\
\vdots & & & \ddots & & \ddots & & & & \vdots \\
0 & 0 & \dots & & M_{\mathbf{r}_{o_{n-1}}} & M_{t_{o_{n-1}}} & M_{\mathbf{r}_{p_{n-1}}} & M_{t_{p_{n-1}}} & M_{\mathbf{r}_{f_{n-1}}} & M_{t_{f_{n-1}}} \\
\hline
\mathbf{I} & \vec{0} & \mathbf{0} & \vec{0} & \dots & \dots & \mathbf{0} & \vec{0} & -\mathbf{I} & \vec{0} \\
-\mathbf{B}_{2,1}^{-1}\mathbf{A}_{2,1} & \vec{a}_1 + \dots & \mathbf{B}_{2,1}^{-1} & -\mathbf{B}_{2,1}^{-1}\vec{v}_2^- & \dots & \dots & -\mathbf{B}_{n-1,n}^{-1} & \mathbf{B}_{n-1,n}^{-1}\vec{v}_{n-1}^+ & \mathbf{B}_{n-1,n}^{-1}\mathbf{A}_{n-1,n} & -\vec{a}_n - \dots \\
 & \mathbf{B}_{2,1}^{-1}\mathbf{A}_{2,1}\vec{v}_1 & & & & & & & & \mathbf{B}_{n-1,n}^{-1}\mathbf{A}_{n-1,n}\vec{v}_n \\
\mathbf{0} & -1 & \mathbf{0} & 0 & \dots & \dots & \mathbf{0} & 0 & \mathbf{0} & 1
\end{array}\right]
$$

Using Eq. 14, the postions of the patch points are updated. This makes the trajectory discontinuous in position again. Therefore, the MSDC algorithm returns to the first level of the algorithm to make the trajectory continuous in position. The second level is then used to update the positions again for a trajectory closer to a continuous trajectory in velocity. It iterates over these two levels of the algorithm until the Euclidean error of $-\Delta\mathbf{v}$ and the constraints are below 10^{-4}. The result of the iterative process is shown in Figure 8.

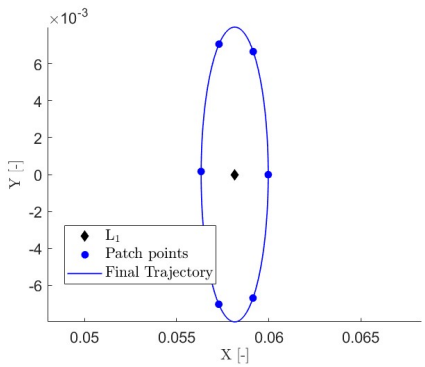

Fig. 8 Final solution for the trajectory of a periodic orbit around L_1

4. Initial Guess

Due to the eccentricity of the ER3BP, the periodic orbit is restricted in terms of the period of the orbit. These extra constraints make it hard to find a suitable initial guess that can be converged by the MSDC into a periodic orbit, immediately. Therefore, the initial guess is done in the CR3BP. Using the continuation method which is explained in Sec. IV.A.5, a family of periodic orbits is identified with the constraint for T_1 in CR3BP. In Figure 9, a family of periodic orbits around L_1 is shown, where two periodic orbits are identified that satisfy the constraint $T_1 = \frac{2m\pi}{n}$. The

red orbit has a period of 2π and the blue orbit has a period of π. In Figure 9b, all the periods of the orbits that are displayed in Figure 9a are shown. Here, more orbits satisfy the constraint for T_1, for example $T_1 = \frac{3}{2}\pi$. However, in this paper only periodic orbits with m=1 are considered. In Figure 9b, a horizontal line is added to show where the orbits satisfy $T_1 = \frac{2\pi}{N}$. The same has been done for Lyapunov orbits around L_2 and L_3, which are shown in Figures 10 and 11, respectively. In both cases, only one orbit satisfies the period constraint with periods of 2π.

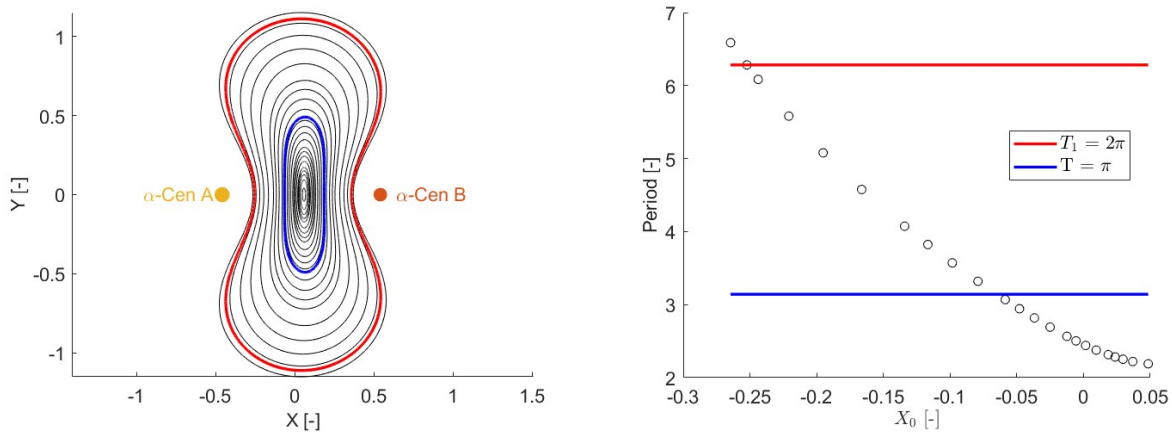

(a) **(b)**

Fig. 9 Family of periodic orbits around L_1 in the classical CR3BP

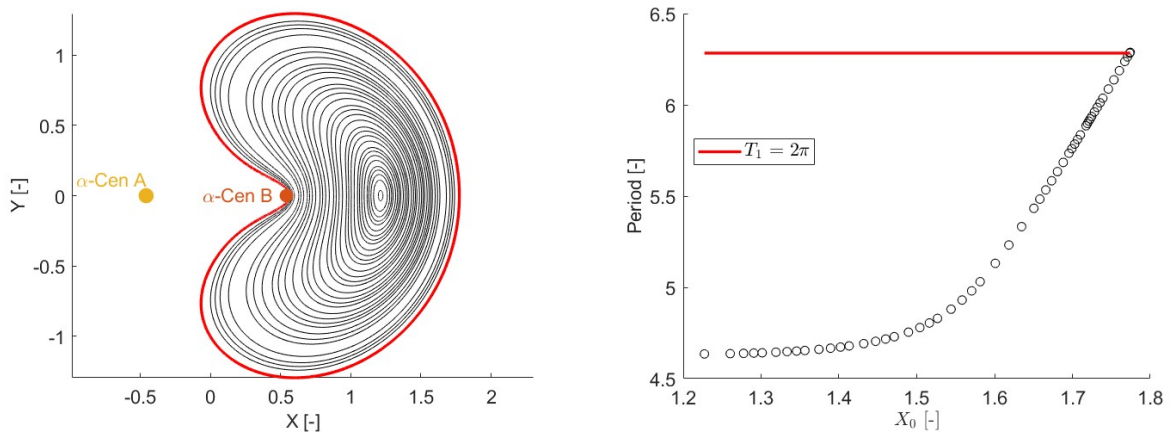

(a) **(b)**

Fig. 10 Family of periodic orbits around L_2 in the classical CR3BP

The continuation method is used to increase the eccentricity. In the initial guess, the lightness number β is also set to zero, which means that there is no PRP acceleration present. This is done to have some freedom in the orientation of the photon sail once a periodic orbit has been found in the classical ER3BP. Using the continuation method, multiple periodic orbits for varying orientations of the photon sail can be identified.

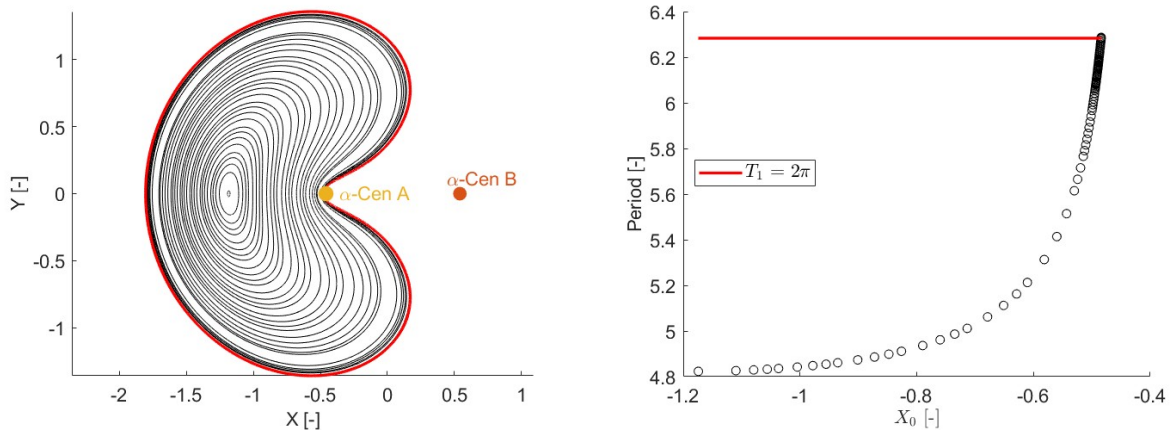

(a) Trajectories **(b) Periods**

Fig. 11 Family of periodic orbits around L_3 in the classical CR3BP

5. Continuation method to increase eccentricity and photon-pressure acceleration

Using the continuation method, both eccentricity and PRP acceleration are slightly increased to find periodic orbits in the PRP-augmented ER3PB. A continuation method can be used to slowly increase a parameter while using the MSDC. In previous research, the continuation method has been used to design a family of periodic orbits, where the initial conditions are slightly changed [15],[31],[17]. Furthermore, parameters such as PRP acceleration [22],[32],[33],[34],[35] or eccentricity [21],[36] can be increased in small steps. First, the eccentricity is slightly increased since this is a fixed constraint in the system. In Section II, it was already mentioned that the eccentricity of the system is equal to $e = 0.5208$. The eccentricity is increased with steps of 0.001 to reach the required eccentricity of the system. The states of the patch points before the use of MSDC for the next step in eccentricity $\mathbf{X}_{e,0}$ is determined by looking at the final solution of the previous steps. The following relation is used to find the initial states $\mathbf{X}_{e,0} = \mathbf{X}_{e-1,f} + (\mathbf{X}_{e-1,f} - \mathbf{X}_{e-2,f})$. Here, the subscripts $(e-1, f)$ and $(e-2, f)$ refer to the converged solution at the two previous eccentricities. If the system does not converge, smaller increments of eccentricity are used. Once the continuation method has reached the required eccentricity, the same method can be used to increase the photon-pressure acceleration. This is done by slightly increasing the lightness number. The continuation method is used to slightly increase the lightness number with steps of $\Delta\beta_{\odot} = 10^{-4}$ until it reaches a maximum lightness number for which the MSDC algorithm converges to a solution. If the algorithm continues to converge for larger lightness numbers, a maximum of $\beta = 2$ is defined.

B. Results of planar Lyapunov orbits

The set of colored Lyapunov orbits in Figures 9 - 11 are used to identify periodic orbits in the ER3BP by slowly increasing the eccentricity of the system. As the orbit becomes dependent on the true anomaly of the system, the

periodic orbit around L_1 with a period of π needs to orbit twice to make it periodic in the ER3BP as well. Next, the true anomaly at the start of the orbit (θ_0) should remain constant. To do that, the start of the orbit is defined as the point where the orbit passes through the $\hat{\mathbf{x}}$-axis. This occurs twice in a periodic orbit with a period of 2π in the CR3BP and four times for an orbit with a period of π in the CR3BP. Changing the value of θ_0 results in a different periodic orbit in the ER3BP. This means that there are an infinite number of periodic orbits. In this article, two values of θ_0 are investigated: $\theta_0 = 0$ and $\theta_0 = \pi$. Therefore, a set of 8 different periodic orbits around the colinear Lagrange points has been designed in the classical ER3BP. In Figure 12, the four Lyapunov orbits around L_1 are shown. In Figure 12a, the trajectories with $T_1 = 2\pi$ are shown and in Figure 12b, the trajectories with $T_1 = \pi$ are shown. Figure 13 contains the four trajectories in ER3BP around L_2 and L_3.

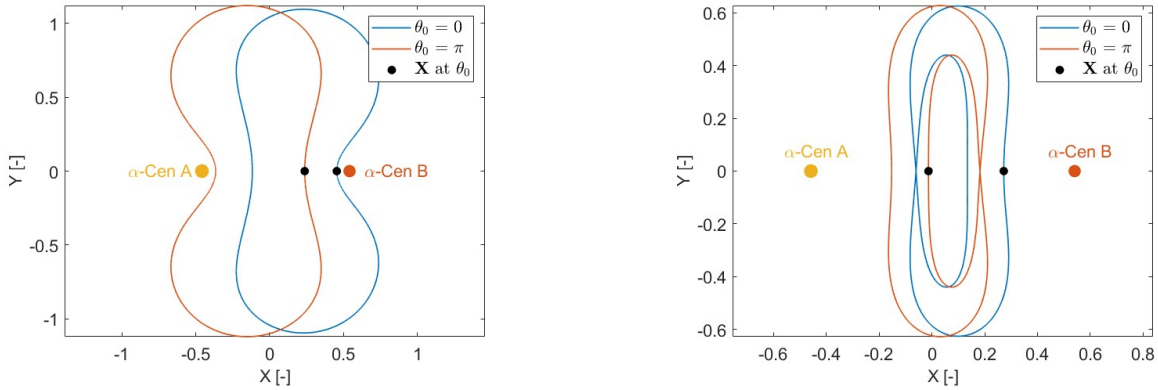

(a) $T_1 = 2\pi$ **(b)** $T_1 = \pi$

Fig. 12 Lyapunov orbits around L_1 in ER3BP with varying θ_0

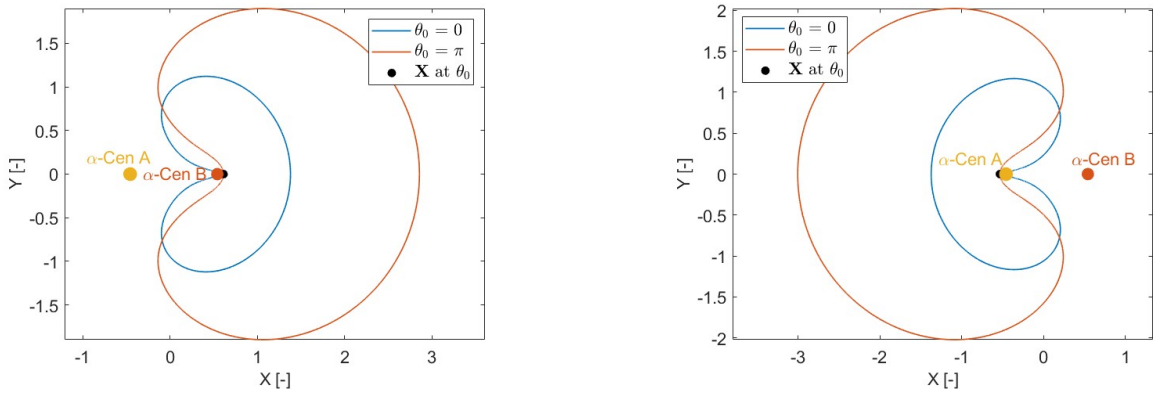

(a) L_2 **(b)** L_3

Fig. 13 Lyapunov orbits around L_2 and L_3 in ER3BP with varying θ_0

The periodic orbits have been identified in the classical ER3BP of the α-Cen system. Next, the photon-sail acceleration is added using the same continuation method to increase the lightness number of the sail. Therefore, a set of

constant steering laws of the sail must also be defined. Due to the fact that only planar Lyapunov orbits are considered, the clock angle δ is set to 90 deg to ensure that the photon-sail acceleration in the $\hat{\mathbf{z}}$-direction is zero. Besides that, the cone angle α is set to a constant value of 0 and 90 deg. The cone angle is defined in frame $\mathcal{A}$ and $\mathcal{B}$, resulting in a set of four constant steering laws, α_A = 0 deg, α_A = 90 deg, α_B = 0 deg and α_B = 90 deg. Lastly, a fifth constant steering law is added in which the normal vector of the sail is set to always point in the direction parallel to the $\hat{\mathbf{y}}$-axis. The constant cone angle could have been set to any number, resulting in an infinite number of available periodic orbits. In this paper, five constant steering laws have been investigated, resulting in a set of 5x8 = 40 periodic orbits in the PRP-augmented ER3BP. Using the continuation method to increase the lightness number to a defined maximum of β = 2, the maximum lightness numbers achieved β_{max} for the entire set are shown in Table 3.

Table 3 Maximum achievable lightness number of PRP-augmented Lyapunov orbits for different constant steering laws. Table is coloured using Green: $\beta = 2$, Blue: $V_{max} \rightarrow 0$ and Yellow: $V_{max} \rightarrow \infty$

Lagrange Point (T_1)	θ_0 **= 0**					$\theta_0 = \pi$				
	α_A **[deg]**		α_B **[deg]**			α_A **[deg]**		α_B **[deg]**		
	0	**90**	**0**	**90**	$\hat{\mathbf{n}}$ **= [0 1 0]**	**0**	**90**	**0**	**90**	$\hat{\mathbf{n}}$ **= [0 1 0]**
L_1 **(2π)**	0,7277	0,6188	1,0252	2	2	0,7276	2	0,9302	0,1903	2
L_1 **(π)**	0,7277	2	1,0544	2	2	0,7277	2	0,9032	2	2
L_2	0,2661	0,2091	1,8641	0,1131	0,1353	0,6739	2	1,8628	0,5596	2
L_3	0,7272	0,2444	0,844	0,0631	0,0539	0,7274	1,4528	0,7275	2	0,2773

In this table, the three colours represent three different types of Lyapunov orbits. First, the constant steering laws that reach β_{max} = 2 are shown in green. The steering laws shown in yellow and blue cannot achieve β = 2. When the lightness numbers for the steering laws in blue are increased, the Lyapunov orbits shrink in size. This also causes the maximum velocity of the orbit to decrease as lightness numbers increase. On the other hand, the maximum velocity of the orbits with the steering laws in yellow in Table 3 increases with higher lightness numbers. Eventually, the maximum velocity tends to go to infinity, resulting in a maximum lightness number below β = 2. In Figure 14, these three types of Lyapunov orbits are shown. In Figure 14a, the orbital trajectories with their β_{max} are shown. In Figure 14b, the corresponding maximum velocities V_{max} of the Lyapunov orbits are shown for different lightness numbers. The same is shown for Lyapunov orbits around L_2 in Figure 15. The trajectories and the corresponding V_{max} for all 40 orientations are added in Appendix B of the main report. It can be seen that for the expanding Lyapunov orbits, V_{max} eventually tends to go to infinity. If the Lyapunov orbit converges towards one of the stars, the PRP-acceleration keeps decelerating the spacecraft. Eventually, the maximum velocity goes to V_{max} = 0, resulting in an artificial equilibrium point. On the other hand, if the amplitude decreases while $\hat{\mathbf{n}}$ is not placed parallel to one of the stars, the PRP acceleration minimises once the orbit stays close to the $\hat{\mathbf{x}}$-axis. This means that the effect of increasing the lightness number is minimised for larger values of β.

Some patterns can be observed in Table 3 and Figures 14 and 15. The Lyapunov orbits around L_1, with steering

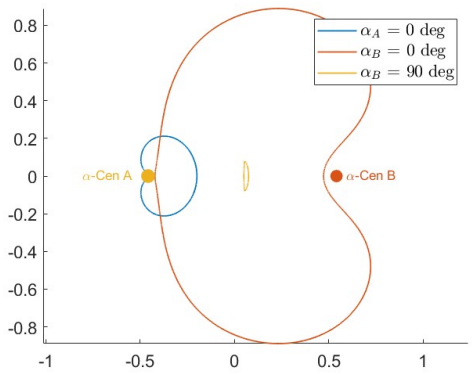

(a) Lyapunov orbits for achieved β_{max}

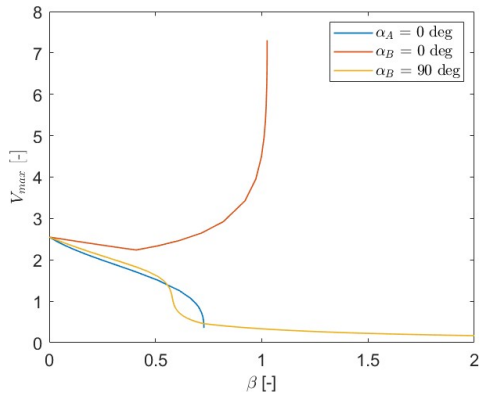

(b) V_{max} for increasing lightness number

Fig. 14 PRP-augmented Lyapunov orbits around L_1 with $T_1 = 2\pi$ and $\theta_0 = 0$

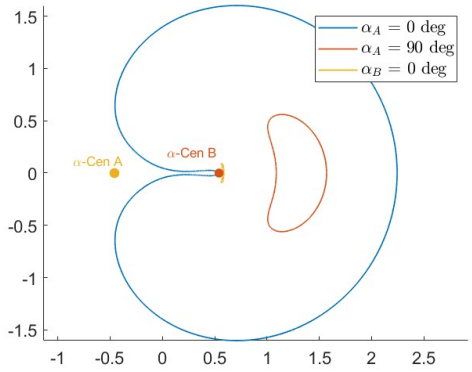

(a) Lyapunov orbits for achieved β_{max}

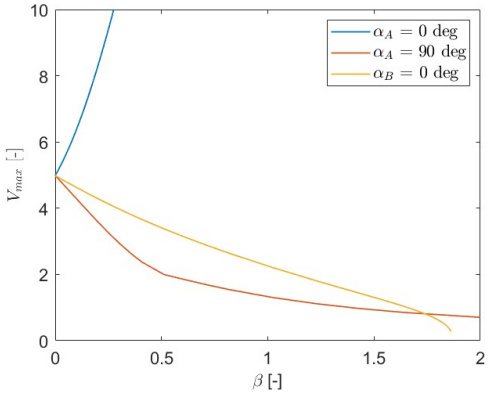

(b) V_{max} for increasing lightness number

Fig. 15 PRP-augmented Lyapunov orbits around L_2 with $\theta_0 = \pi$

laws in which the normal vector is pointed perpendicular to the stellar arrays when passing the $\hat{\mathbf{x}}$-axis often result in a β_{max} of 2. When this axis is passed, the spacecraft is closest to one of the primary bodies, resulting in a relatively large PRP acceleration. This orientation occurs when the normal vector is kept at $\hat{\mathbf{n}} = [0\ 1\ 0]$. In addition to that, it also occurs for α_A and $\alpha_B = 90$ deg. However, for the Lyapunov orbit around L_1 with $T_1 = 2\pi$, the solar acceleration is still too large for two steering laws. Looking at Figure 12a, setting $\alpha_A = 90$ deg results in the normal vector being almost parallel to the photon rays from α-Cen B when the spacecraft is (almost) above or below α-Cen B. For the Lyapunov orbit with $\theta_0 = 0$, the spacecraft is relatively close to α-Cen B. Therefore, the combination of having the normal vector parallel to the photon rays and being close to the star results in a too large PRP acceleration. The same occurs for the Lyapunov orbit with $\theta_0 = \pi$ and the orientation of $\alpha_B = 90$ deg.

The Lyapunov orbits around L_2 and L_3 in the classical ER3BP with $\theta_0 = 0$ are very close to α-Cen A or B. This causes the amplitude of the orbit to increase. However, if the normal vector of the sail is placed parallel to the photon

rays of the closest star, the orbit decreases until it converges to an AEP. For all other orientations, V_{max} goes to infinity as the orbit increases towards the star. Initiating the Lyapunov orbit at $\theta_0 = \pi$, results in a larger distance to the stars in the classical ER3BP, as shown in Figure 13. If the normal vector is (almost) parallel to the $\hat{\mathbf{y}}$-axis, the PRP acceleration is large enough for the orbit to decrease in size, not too large for V_{max} to converge to 0. Therefore, the Lyapunov orbits around L_2 with $\alpha_A = 90$ deg and $\hat{\mathbf{n}} = [0\ 1\ 0]$, result in $\beta_{max} = 2$. For Lyapunov orbits around L_3, only $\alpha_B = 90$ deg reaches $\beta_{max} = 2$. The orientation $\hat{\mathbf{n}} = [0\ 1\ 0]$ converges toward an AEP at $\beta_{max} = 0.277$.

Another pattern that can be observed in Table 3 is that most of the orientations where V_{max} converge to 0 have a β_{max} close to 0.727. This can be explained by looking at the required lightness number for an AEP, in Figure 16 [12]. There is a contour line around α-Cen A which requires a lightness number of approximately 0.7. Therefore, the orientations for which the Lyapunov orbits decrease towards α-Cen A will converge into an AEP with a value of $\beta_{max} = 0.727$. Next to that, two Lyapunov orbits around L_2 converge towards an AEP with $\beta_{max} = 1.86$. These orbits decrease toward α-Cen B, which has a contour line of $\beta = 1.8$ around it. The last orientation that converges to $V_{max} = 0$ is a Lyapunov orbit around L_3 with $\hat{\mathbf{n}} = [0\ 1\ 0]$. Looking at the required normal vectors in Figure 16, this orientation occurs at approximately x = 0. At y = ± 0.8, there are contour lines in the range of 0.2, which corresponds to the achieved $\beta_{max} = 0.277$.

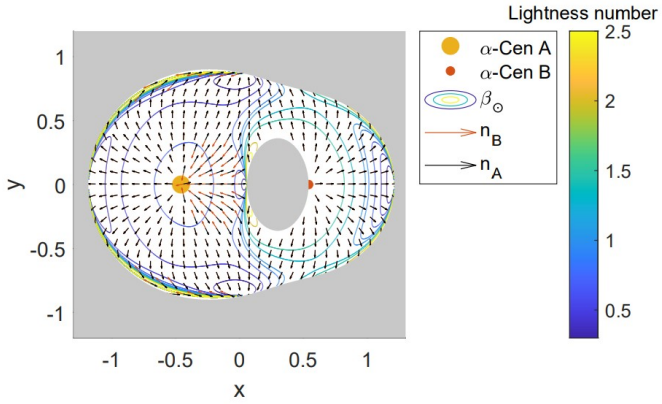

Fig. 16 Required lightness number to create an artificial equilibrium point for a two-sided photon sail [12]

Lyapunov orbits with $\theta_0 = \pi$ have a higher chance of reaching $\beta_{max} = 2$ for orbits around L_2 and L_3. Here, the periodic orbits in the classical ER3BP orbit relatively close to one of the stars at the beginning of the orbit. In the pulsating frame $\mathcal{S}_{\mathcal{P}}$, the position vector remains constant regardless of the true anomaly. However, in the real situation, the position vector is maximum at $\theta = \pi$. Looking at the Lyapunov orbits around L_1, the distances towards the stars are much larger, which means that the change in the true anomaly does not have such a great effect.

V. Trajectories between two periodic orbits

To further explore the α-Cen system, this section investigates the design of trajectories between the periodic orbits in Section IV. This is done using an evolutionary algorithm, as it does not require a priori knowledge of the problem.

A. Evolutionary Algorithm

In low-energy transfers, genetic algorithms and differential evolution schemes are widely used [12][37]. In comparison, a differential evolution algorithm is a simpler method than a genetic algorithm, while it can achieve better results [38]. In a differential evolution (DE) algorithm, each generation consists of a population with size N_{pop}. Each individual i in the population is a decision vector of size N_{par}, which represents the number of parameters. A suitable value of N_{pop} can be determined using [39]

$$N_{pop} = \text{ceiling}\left(\frac{\ln(1-0.5^{1/N_{par}})}{\ln(1-0.17)}\right) \tag{32}$$

The values of the parameters can change when proceeding to the next generation to find the most optimal solution to the problem. From the population, three 'parent' vectors are randomly selected, which are denoted as $\mathbf{V}_1$, $\mathbf{V}_2$ and $\mathbf{V}_3$. To proceed to the next generation, each parameter j mutates with a chance of CR%, which is the crossover probability. In a standard DE, if the parameter mutates, the 'child' vector $\mathbf{u}$ is determined using [40]

$$\mathbf{u}_{i,j} = \mathbf{V}_{1,j} + F(\mathbf{V}_{2,j} - \mathbf{V}_{3,j}) \tag{33}$$

Here, F is the scaling factor. If 'child' vector $\mathbf{u}_i$ results in a more optimal solution than 'parent' vector $\mathbf{V}_i$, the 'child' vector will replace the 'parent' vector. In this algorithm, CR and F are problem-specific control parameters that require tuning to find the optimal values for a standard DE algorithm. A new adaptive DE algorithm is available to update the control parameters during the optimisation process. This adaptive DE algorithm is called JADE [41] and is proven to achieve faster optimal solutions [40]. In this algorithm, a fourth parent vector $\mathbf{V}^p_{best,j}$ is randomly chosen of the $100p$% best parents. Here, p is a constant value between 0 and 1. The four parent vectors are then used to determine the child vector using

$$\mathbf{u}_{i,j} = \mathbf{V}_{1,j} + F(\mathbf{V}^p_{best,j} - \mathbf{V}_{1,j}) + F(\mathbf{V}_{2,j} - \mathbf{V}_{3,j}) \tag{34}$$

The JADE algorithm adapts the values of CR and F at each generation. The value CR is a random number from the normal distribution with a mean μ_{CR} and a standard deviation of 0.1. The mean starts with $\mu_{CR} = 0.5$ and is updated after every generation using

$$\mu_{CR} = (1 - c)\mu_{CR} + \text{mean}_A(S_{CR}) \tag{35}$$

Here, c is a constant parameter which is chosen at the start of the first generation. Mean_A is the arithmic mean and S_{CR} is the set of all the crossover probabilities, for which the child vector was more successful than its parent. The scaling factor F is also updated after every generation, by choosing a random number from the Caucy distribution with μ_F as location parameter and 0.1 as scale parameter. Again, μ_F is initiated with a value of 0.5 and then updated after every generation using

$$\mu_F = (1 - c)\mu_F + \text{mean}_L(S_F) \tag{36}$$

The set of successful values for F is denoted with S_F and mean_L represents the Lehmer mean. This Lehmer mean is calculated using

$$\text{mean}_L = \frac{\sum_{F \in S_F} F^2}{\sum_{F \in S_F} F} \tag{37}$$

In this algorithm, two new parameters are introduced that are non-specific to the problem. These parameters are c, which controls the parameter adaptation and p, which controls the greediness of the mutation. Both parameters are set to 0.1 in this problem based on a trial-and-error method.

The method of using an evolutionary algorithm to find trajectories between two periodic orbits is based on the method of Heiligers [12]. This method was used to find heteroclinic-like trajectories between two artificial equilibrium points in α-Cen, but it can also be used for trajectories between periodic orbits [32]. To design such trajectories, the trajectory is divided into two segments, the departure and arrival trajectory. The first trajectory will be denoted using the subscript 'D', and the latter will be denoted by the subscript 'A'. The departure trajectory is numerically propagated from the departure point P_D over a time span $\theta_{D,0}$. Both P_D and $\theta_{D,0}$ are determined by the JADE algorithm. This starting point lies along a periodic orbit that has been designed in Section IV.A, and the state at P_D is denoted as $\mathbf{x}_{D,0}$. The trajectory is propagated forward from $\mathbf{x}_{D,0}$ with a piecewise constant photon-sail attitude. These attitudes are described by a set of cone angles, denoted as $\boldsymbol{\alpha}_D = [\alpha_{D,1}\ \alpha_{D,2}\ \dots\ \alpha_{D,f}]$. The arrival segment is propagated backward starting from the arrival point P_A with state vector $\mathbf{x}_{A,0}$ at time $\theta_{A,0}$. Along the arrival segment, a similar set of cone angles, $\boldsymbol{\alpha}_A = [\alpha_{A,1}\ \alpha_{A,2}\ \dots\ \alpha_{A,f}]$ is employed. The time intervals in which these cone angles are constant are denoted in the vector $\boldsymbol{\theta}_\alpha = [\theta_{D,1}\ \theta_{D,2}\ \dots\ \theta_{D,f}\ \theta_{A,1}\ \theta_{A,2}\ \dots\ \theta_{A,f-1}]$. These parameters result in a decision vector $\mathbf{v} = [\theta_{D,0}\ \theta_{A,0}\ \boldsymbol{\alpha}_D\ \boldsymbol{\alpha}_A\ \boldsymbol{\theta}_\alpha]$. The JADE algorithm is used to find the most optimal trajectory, which is defined as the trajectory where the Euclidean distance between the state vectors at the end of the two segments is minimal. Therefore, the objective of the algorithm is to find a vector $\mathbf{v}$ where $||\mathbf{x}_{D,f} - \mathbf{x}_{A,f}||$ is minimal.

A time constraint is added to the problem due to the eccentricity of the α-Cen system. When arriving at P_A, not only should the state of the trajectory coincide with the state of the periodic orbit, but also the true anomaly of the system should be the same. This is the reason why the vector $\boldsymbol{\theta}_\alpha$ does not contain $\theta_{A,f}$. The parameter $\theta_{A,f}$ is constrained and can be calculated using

$$\theta_{A,f} = \theta_{A,0} - \theta_{D,0} - \text{sum}(\boldsymbol{\theta}_\alpha) \tag{38}$$

B. Results

To investigate whether trajectories between the designed planar Lyapunov orbits in Section IV exist, a fixed departure orbit has been chosen. Two different arrival orbits have been chosen to investigate the effect of θ_0 on the trajectory. As the goal of the trajectories is to explore α-Cen further, a combination of orbits around L_2 and L_3 have been considered as they span the entire system. As a departure orbit, the planar Lyapunov orbit around L_2, with a cone angle of $\alpha_B = 0$ deg and $\theta_0 = 0$. The lightness number has been set to 0.1, as this value is futuristic, but is expected to be achievable. The first arrival periodic orbit has been set to a planar Lyapunov orbit around L_3, with a constant cone angle of $\alpha_B = 0$ deg for $\theta_0 = 0$. To be able to find a continuous trajectory from one orbit into the next, the lightness number needs to be constant as well. Therefore, the lightness numbers of the arrival orbit and of the trajectory itself are also set to 0.1. However, to investigate the effect of the lightness number on the trajectory, a second photon-sail trajectory with $\beta = 0.5$ is identified. The departure and arrival orbits remain the same, so with $\beta = 0.1$, to isolate the effect of the lightness number on the trajectory. A higher lightness number is expected to increase the maneuverability of the spacecraft. Therefore, one segment is used in the departure and arrival leg for $\beta = 0.5$. For $\beta = 0.1$, three segments are used in both the departure and arrival leg. The algorithm is run for 2500 generations and is repeated five times using five different random seeds. The most optimal results of the JADE algorithm are shown in Figure 17. Here, in Figure 17a the trajectory with $\beta = 0.1$ and in Figure 17b the trajectory with $\beta = 0.5$ are shown. It can be seen that the trajectory with $\beta = 0.1$ is relatively close to α-Cen A. It uses this star as a gravity assist to reach the arrival orbit. Comparing this to the trajectory with $\beta = 0.5$, the trajectory stays farther away from the stars and mainly uses the PRP acceleration to arrive at the second orbit. The characteristics of the trajectories are given in Table 4. The Euclidean error $||\mathbf{x}_{D,f} - \mathbf{x}_{A,f}||$ for the trajectory with $\beta = 0.1$ has a relatively high value of 0.071. A solar sail with $\beta = 0.5$ can more easily 'steer' through the stellar system, resulting in a continuous trajectory with a Euclidean error of 2.39E-7. It can be assumed that this trajectory is continuous. Not only the Euclidean error is smaller, but also the required TOF is shorter.

The same has been done for a different arrival orbit to see whether changing the θ_0 of the Lyapunov orbit has an effect on the trajectory. Therefore, the new arrival orbit is around L_3, with $\alpha_B = 90$ deg and $\theta_0 = \pi$. The two trajectories with varying β are shown in Figure 18. Again, the trajectory with $\beta = 0.5$ achieves a negligible dimensionless Euclidean

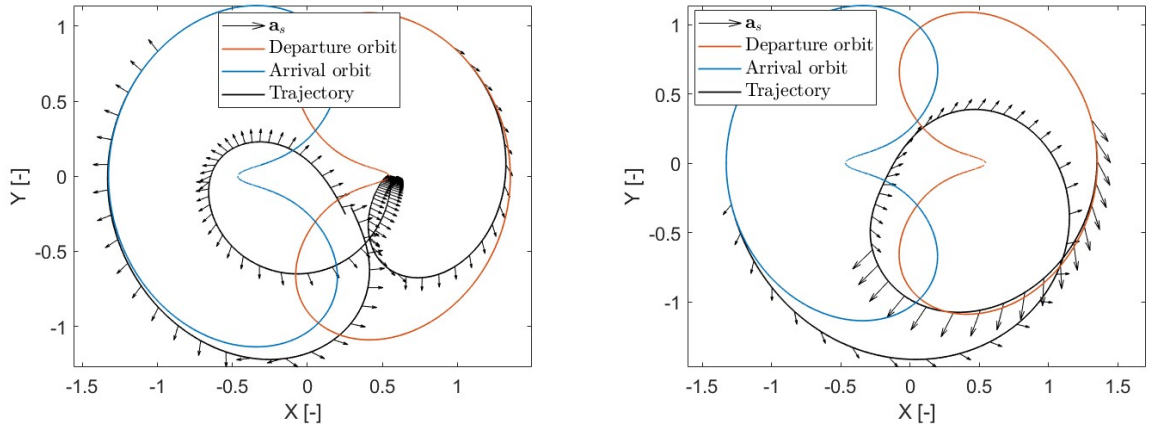

(a) β of trajectory = 0.1 **(b) β of trajectory = 0.5**

Fig. 17 Trajectory between departure orbit: L_2 with α_B = 0 deg and θ = 0 and the arrival orbit: L_3 with α_B = 0 deg and θ_0 = 0. Both Lyapunov orbits have lightness number β = 0.1

error of 1.65E-8, resulting in a continuous trajectory. The trajectory with $\beta = 0.1$ has a Euclidean error of 0.004, which is better compared to the trajectory in Figure 17, but not small enough to assume a continuous trajectory. Again, the characteristics of the two trajectories are shown in Table 4.

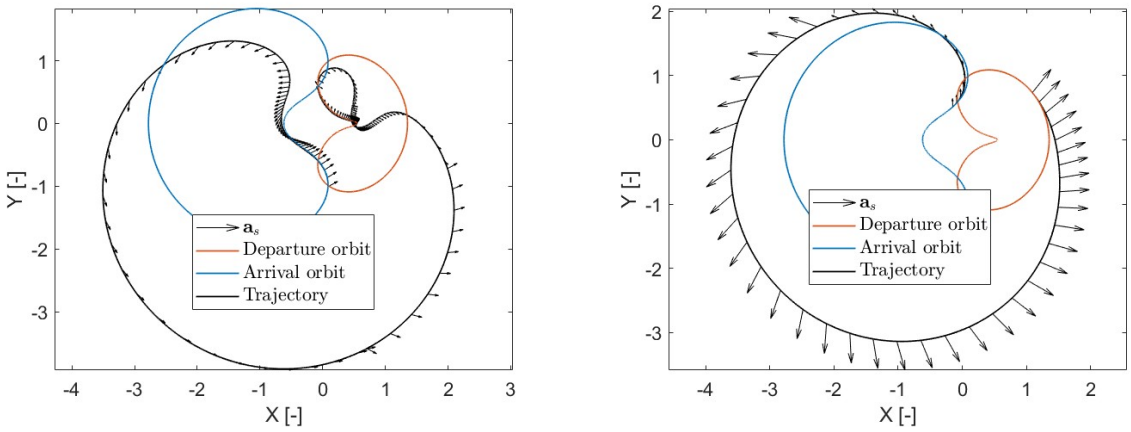

(a) Lyapunov orbits for achieved β_{max} **(b) V_{max} for increasing lightness number**

Fig. 18 Trajectory between departure orbit: L_2 with α_B = 0 deg and θ = 0 and the arrival orbit: L_3 with α_B = 90 deg and $\theta_0 = \pi$. Both Lyapunov orbits have lightness number β = 0.1

The main difference between the trajectories in Figures 17 and 18 is that the latter trajectories are mostly outside the periodic orbits, while the trajectories in the former stay within the stellar system. Both trajectories in Figure 17 even go between α-Cen A and B. To explore most of the system best, travelling between the stars gives a unique view of the system.

Lastly, a trajectory from L_2 to L_3 is designed with $\beta = 2$. The sail in both the Lyapunov orbits and the trajectory

has this lightness number. This trajectory is shown in Figure 19. Due to the high lightness number, the spacecraft has high maneuverability, which again results in a small Euclidean error. The characteristics of this trajectory are shown in the last row of Table 4. The dimensionless Euclidean error is negligible, and the TOF of the trajectory is significantly shorter compared to the other trajectories, caused by the high lightness number.

So, the results show that the JADE algorithm can identify continuous trajectories between planar Lyapunov orbits, with negligible Euclidean errors between the departure and arrival legs. For lower lightness numbers, the algorithm converges to a trajectory with a larger Euclidean error and also uses the stars for a gravity assist. In further research, the designed trajectories can be used as an initial guess in a modified MSDC algorithm. For the lower lightness numbers, the MSDC can further decrease the Euclidean error. Using an additional time constraint, the MSDC can also decrease the TOF of the trajectory by using a continuation method to slowly decrease this time constraint.

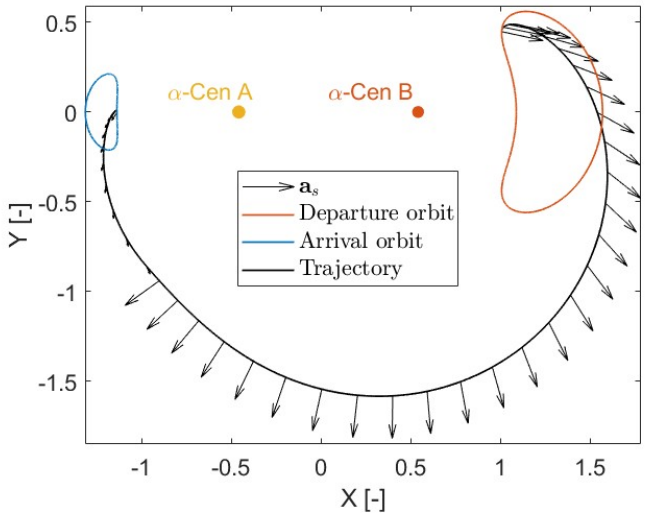

Fig. 19 Trajectory between departure orbit around L_2 with α_A = 90 deg and $\theta_0 = \pi$ and the arrival orbit around L_3 with α_B = 90 deg and $\theta_0 = \pi$. Lightness number of the periodic orbits and the trajectory is β = 2

Table 4 Characteristics of five different trajectories between two planar Lyapunov orbits

Departure Orbit	$\theta_{0,D}$	**Arrival Orbit**	$\theta_{0,D}$	β	$\theta_{A,0}$	α_D **[deg]**	α_A **[deg]**	$\theta_{\alpha,D}$	$\theta_{\alpha,A}$	$\|\|\mathbf{x}_{D,f} - \mathbf{x}_{A,f}\|\|$	**TOF**
L_2, $\alpha_B = 0$	0	L_3, α_B = 0 deg	0	0.1	0.75π	$\begin{bmatrix}-62.1\\-12.9\\27.2\end{bmatrix}$	$\begin{bmatrix}5.26\\-87.7\\41.0\end{bmatrix}$	$\begin{bmatrix}0.57\\0.55\\0.24\end{bmatrix}\pi$	$\begin{bmatrix}0.66\\0.07\\0.39\end{bmatrix}\pi$	0.071	2.48π
L_2, $\alpha_B = 0$	0	L_3, α_B = 0 deg	0	0.5	0.92π	-62.6	30.7	0.75π	1.25π	2.39E-7	2.01π
L_2, $\alpha_B = 0$	0	L_3, α_B = 90 deg	π	0.1	2π	$\begin{bmatrix}62.3\\-90\\-32.9\end{bmatrix}$	$\begin{bmatrix}89.8\\86.4\\44.9\end{bmatrix}$	$\begin{bmatrix}0.28\\0.57\\0.47\end{bmatrix}\pi$	$\begin{bmatrix}1.56\\0.003\\0.39\end{bmatrix}\pi$	0.0044	3.28π
L_2, $\alpha_B = 0$	0	L_3, α_B = 90 deg	π	0.5	0.80π	26.0	33.2	1.55π	0.53π	1.65E-8	2.09π
L_2, $\alpha_A = 90$	π	L_3, α_B = 90 deg	π	2	0.35π	-29.1	57.5	1.26π	0.39π	2.25E-8	1.65π

VI. Conclusions

In this paper, a number of PRP-augmented planar Lyapunov orbits around the colinear Lagrange points of Alpha Centauri have been designed using an MSDC algorithm. Around the L_1 point, periodic orbits with a period of π and 2π exist in the CR3BP. For Lyapunov orbits around L_2 and L_3, only orbits with a period of 2π exist. These four periodic orbits in the ER3BP are used as input in the continuation method to increase the lightness number. As the elliptical model depends on the true anomaly of the system, the true anomaly is kept constant at the start of the orbit. This constant value is set to $\theta_0 = 0$ and $\theta_0 = \pi$ to investigate the effect of starting the periodic orbit at a different moment. When the lightness number is increased, the orientation of the photon sail is kept constant in a set of five different constant steering laws, being $\alpha_A = 0$ deg, $\alpha_A = 90$ deg, $\alpha_B = 0$ deg, $\alpha_B = 90$ deg and $\hat{\mathbf{n}} = [0\ 1\ 0]$. The lightness number is increased until the MSDC algorithm does not converge anymore or if the lightness number reaches a defined maximum value of 2. If the lightness number does not reach a value of 2, the maximum velocity converges to 0 or tends to go to infinity. Orientations that constantly orient $\hat{\mathbf{n}}$ parallel to the rays of the closest star result in a V_{max} of 0. The PRP acceleration causes the Lyapunov orbit to keep decreasing in size until it converges into an AEP. Therefore, β_{max} corresponds to the lightness number required to create an AEP close to the star. Orienting the sail in such a way that $\hat{\mathbf{n}}$ is $[0\ 1\ 0]$ when passing the $\hat{\mathbf{x}}$-axis, the PRP acceleration in the $\hat{\mathbf{x}}$-direction is limited because that is the moment when the photon sail is closest to the star. Having enough PRP acceleration in the $\hat{\mathbf{y}}$-direction results in a decreasing size of the periodic orbit. The PRP acceleration becomes smaller as the size of the orbit decreases. Therefore, V_{max} converges to a value larger than 0 for increasing lightness numbers. These orientations result in $\beta_{max} = 2$. If the orientation causes the PRP acceleration in either direction to become too large or too small, V_{max} increases for larger lightness numbers and eventually reaches $V_{max} \rightarrow \infty$.

The planar Lyapunov orbits around L_2 and L_3 in the classical ER3BP are very close to the two primary bodies, for $\theta_0 = 0$. For that reason, periodic orbits increase in size when the lightness number increases, resulting in V_{max} going to infinity. Only if $\hat{\mathbf{n}}$ is pointed parallel to the closest primary body, the PRP acceleration is large enough to converge the Lyapunov orbits into an AEP. For another initial true anomaly, $\theta_0 = \pi$ the Lyapunov orbits are larger and further away from the primary bodies. Again, orienting $\hat{\mathbf{n}} = [0\ 1\ 0]$ when passing the $\hat{\mathbf{x}}$-axis results in $\beta_{max} = 2$.

To further explore α-Cen, a trajectory between the identified Lyapunov orbits is designed using the adaptive JADE algorithm. Three different lightness numbers are investigated, $\beta = 0.1$, 0.5 and 2. The trajectory with $\beta = 0.1$ has the highest Euclidean error between the ends of the states of the departure and arrival legs of 0.071 and 0.0044, depending on the arrival orbit. These trajectories also use the stars as a gravity assist as the relatively low lightness number does not create enough maneuverability. The higher lightness numbers of $\beta = 0.5$ and 2 result in a negligible Euclidean error, as it mainly uses the PRP acceleration to travel through the system. When comparing these two larger lightness numbers, the TOF decreases for larger lightness numbers. This TOF can be further reduced by using an MSDC with a time constraint.

References

[1] Kervella, P., Thévenin, F., and Lovis, C., "Proxima's orbit around α Centauri," *Astronomy & Astrophysics*, Vol. 598, 2017, p. L7. https://doi.org/10.1051/0004-6361/201629930.

[2] Anglada-Escudé, G., Amado, P. J., Barnes, J., Berdiñas, Z. M., Butler, R. P., Coleman, G. A. L., de la Cueva, I., Dreizler, S., Endl, M., Giesers, B., Jeffers, S. V., Jenkins, J. S., Jones, H. R. A., Kiraga, M., Kürster, M., López-González, M. J., Marvin, C. J., Morales, N., Morin, J., Nelson, R. P., Ortiz, J. L., Ofir, A., Paardekooper, S.-J., Reiners, A., Rodríguez, E., Rodríguez-López, C., Sarmiento, L. F., Strachan, J. P., Tsapras, Y., Tuomi, M., and Zechmeister, M., "A terrestrial planet candidate in a temperate orbit around Proxima Centauri," *Nature*, Vol. 536, No. 7617, 2016, pp. 437–440. https://doi.org/10.1038/nature19106.

[3] Schoutetens, F., Dachwald, B., and Heiligers, J., "Optimisation of Photon-Sail Trajectories in the Alpha-Centauri System using Evolutionary Neurocontrol," *7th International Conference on Astrodynamics Tools and Techniques*, 2021.

[4] McInnes, C. R., *Solar Sailing*, Springer London, London, 1999. https://doi.org/10.1007/978-1-4471-3992-8.

[5] Tsuda, Y., Mori, O., Funase, R., Sawada, H., Yamamoto, T., Saiki, T., Endo, T., Yonekura, K., Hoshino, H., and Kawaguchi, J., "Achievement of IKAROS — Japanese deep space solar sail demonstration mission," *Acta Astronautica*, Vol. 82, No. 2, 2013, pp. 183–188. https://doi.org/10.1016/j.actaastro.2012.03.032.

[6] Vulpetti, G., Johnson, L., and Matloff, G. L., "The NanoSAIL-D2 NASA Mission," *Solar Sails*, Springer New York, New York, NY, 2015, pp. 173–178. https://doi.org/10.1007/978-1-4939-0941-4{_}16.

[7] Spencer, D. A., Betts, B., Bellardo, J. M., Diaz, A., Plante, B., and Mansell, J. R., "The LightSail 2 solar sailing technology demonstration," *Advances in Space Research*, Vol. 67, No. 9, 2021, pp. 2878–2889. https://doi.org/10.1016/j.asr.2020.06.029.

[8] Macdonald, M., and McInnes, C., "Solar sail science mission applications and advancement," *Advances in Space Research*, Vol. 48, No. 11, 2011, pp. 1702–1716. https://doi.org/10.1016/j.asr.2011.03.018.

[9] Heller, R., Hippke, M., and Kervella, P., "Optimized Trajectories to the Nearest Stars Using Lightweight High-velocity Photon Sails," *The Astronomical Journal*, Vol. 154, No. 3, 2017, p. 115. https://doi.org/10.3847/1538-3881/aa813f.

[10] Heller, R., and Hippke, M., "Deceleration of High-velocity Interstellar Photon Sails into Bound Orbits at α Centauri," *The Astrophysical Journal*, Vol. 835, No. 2, 2017, p. L32. https://doi.org/10.3847/2041-8213/835/2/L32.

[11] Aliasi, G., Mengali, G., and Quarta, A. A., "Artificial equilibrium points for a solar balloon in the α Centauri system," *Acta Astronautica*, Vol. 104, No. 2, 2014, pp. 464–471. https://doi.org/10.1016/j.actaastro.2014.03.006.

[12] Heiligers, J., Schoutetens, F., and Dachwald, B., "Photon-Sail Equilibria in the Alpha Centauri System," *Journal of Guidance, Control, and Dynamics*, Vol. 44, No. 5, 2021, pp. 1053–1061. https://doi.org/10.2514/1.G005446.

[13] Pino, T., and Circi, C., "A star-photon sailcraft mission in the Alpha Centauri system," *Advances in Space Research*, Vol. 59, No. 9, 2017, pp. 2389–2397. https://doi.org/10.1016/j.asr.2017.02.014.

[14] Rotmans, T., "Photon sail trajectories to exoplanet Proxima b using heteroclinic connections," Ph.D. thesis, Delft University of Technology, Delft, 2023.

[15] Grebow, D., "Generating periodic orbits in the circular restricted three body problem with applications to lunar South pole coverage," Ph.D. thesis, Purdue University, West Lafayette, 5 2006.

[16] Goodrich, E. F., "Numerical determination of short-period Trojan orbits in the restricted three-body problem," *The Astronomical Journal*, Vol. 71, 1966, p. 88. https://doi.org/10.1086/109860.

[17] Howell, K. C., and Pernicka, H. J., "Numerical determination of Lissajous trajectories in the restricted three-body problem," *Celestial Mechanics*, Vol. 41, No. 1-4, 1987, pp. 107–124. https://doi.org/10.1007/BF01238756.

[18] Lang, K. R., *The Sun from Space*, Springer Berlin Heidelberg, Berlin, Heidelberg, 2009. https://doi.org/10.1007/978-3-540-76953-8.

[19] Folta, D., Pavlak, T., Haapala, A., and Howell, K., "Preliminary design considerations for access and operations in Earth-Moon L1/L2 orbits," *Advances in the Astronautical Sciences*, Vol. 148, 2013, pp. 2073–2092.

[20] Farrés, A., and Jorba, ., "Periodic and quasi-periodic motions of a solar sail close to SL 1 in the Earth–Sun system," *Celestial Mechanics and Dynamical Astronomy*, Vol. 107, No. 1-2, 2010, pp. 233–253. https://doi.org/10.1007/s10569-010-9268-4.

[21] Ferrari, F., and Lavagna, M., "Periodic motion around libration points in the Elliptic Restricted Three-Body Problem," *Nonlinear Dynamics*, Vol. 93, No. 2, 2018, pp. 453–462. https://doi.org/10.1007/s11071-018-4203-4.

[22] Farres, A., Heiligers, J., and Miguel, N., "Road Map to L4/L5 with a solar sail," *2018 Space Flight Mechanics Meeting*, American Institute of Aeronautics and Astronautics, Reston, Virginia, 2018. https://doi.org/10.2514/6.2018-0211.

[23] Vergaaij, M., and Heiligers, J., "Time-optimal solar sail heteroclinic-like connections for an Earth-Mars cycler," *Acta Astronautica*, Vol. 152, 2018, pp. 474–485. https://doi.org/10.1016/j.actaastro.2018.08.008.

[24] Heiligers, J., Mora, . F., and Farres, A., "Solar-Sail Pathways to the Sun-Earth L5 Point," *5th International Symposium on Solar Sailing*, Aachen, 2019.

[25] Szebehely, V., *Theory of Orbit; The restricted problem of three Bodies*, Elsevier, 1967. https://doi.org/10.1016/B978-0-12-395732-0.X5001-6.

[26] Farrés, A., and Jorba, ., "Station Keeping Strategies for a Solar Sail in the Solar System," 2016, pp. 83–115. https://doi.org/10.1007/978-3-319-27464-5{_}3.

[27] Lockett, T., Johnson, C., Few, A., and Stewart, E., "Lessons Learned from the Flight Unit Testing of the Near Earth Asteroid Scout Flight System," *International Symposium on Solar Sailing*, Aachen, 2019.

[28] Heiligers, J., Fernandez, J. M., Stohlman, O. R., and Wilkie, W. K., "Trajectory design for a solar-sail mission to asteroid 2016 HO3," *Astrodynamics*, Vol. 3, No. 3, 2019, pp. 231–246. https://doi.org/10.1007/s42064-019-0061-1.

[29] Sicardy, B., "Stability of the triangular Lagrange points beyond Gascheau's value," *Celestial Mechanics and Dynamical Astronomy*, Vol. 107, No. 1-2, 2010, pp. 145–155. https://doi.org/10.1007/s10569-010-9259-5.

[30] Grebow, D. J., Ozimek, M. T., Howell, K. C., and Folta, D. C., "Multibody Orbit Architectures for Lunar South Pole Coverage," *Journal of Spacecraft and Rockets*, Vol. 45, No. 2, 2008, pp. 344–358. https://doi.org/10.2514/1.28738.

[31] Parker, J. S., and Anderson, R. L., *Low-Energy Lunar Trajectory Design*, Wiley, 2014.

[32] Heiligers, J., "Homo- and Heteroclinic Connections in the Planar Solar-Sail Earth-Moon Three-Body Problem," *Frontiers in Applied Mathematics and Statistics*, Vol. 4, 2018. https://doi.org/10.3389/fams.2018.00042.

[33] Heiligers, J., Hiddink, S., Noomen, R., and McInnes, C. R., "Solar sail Lyapunov and Halo orbits in the Earth–Moon three-body problem," *Acta Astronautica*, Vol. 116, 2015, pp. 25–35. https://doi.org/10.1016/j.actaastro.2015.05.034.

[34] Heiligers, J., Macdonald, M., and Parker, J. S., "Extension of Earth-Moon libration point orbits with solar sail propulsion," *Astrophysics and Space Science*, Vol. 361, No. 7, 2016, p. 241. https://doi.org/10.1007/s10509-016-2783-3.

[35] Mora, A. F., and Heiligers, J., "Solar-Sail Quasi-Periodic Orbits in the Sun–Earth System," *Journal of Guidance, Control, and Dynamics*, Vol. 43, No. 9, 2020, pp. 1740–1749. https://doi.org/10.2514/1.G005021.

[36] Biggs, J. D., McInnes, C. R., and Waters, T., "Control of Solar Sail Periodic Orbits in the Elliptic Three-Body Problem," *Journal of Guidance, Control, and Dynamics*, Vol. 32, No. 1, 2009, pp. 318–320. https://doi.org/10.2514/1.38362.

[37] Zhang, Y., Peng, L., Dai, G., and Wang, M., "Enhanced Hybrid Differential Evolution for Earth-Moon Low-Energy Transfer Trajectory Optimization," *International Journal of Aerospace Engineering*, Vol. 2018, 2018, pp. 1–17. https://doi.org/10.1155/2018/4560173.

[38] Zuo, M., Dai, G., Peng, L., Tang, Z., Gong, D., and Wang, Q., "A differential evolution algorithm with the guided movement for population and its application to interplanetary transfer trajectory design," *Engineering Applications of Artificial Intelligence*, Vol. 110, 2022, p. 104727. https://doi.org/10.1016/j.engappai.2022.104727.

[39] Clerc, M., and Kennedy, J., "The particle swarm - explosion, stability, and convergence in a multidimensional complex space," *IEEE Transactions on Evolutionary Computation*, Vol. 6, No. 1, 2002, pp. 58–73. https://doi.org/10.1109/4235.985692.

[40] Georgioudakis, M., and Plevris, V., "A Comparative Study of Differential Evolution Variants in Constrained Structural Optimization," *Frontiers in Built Environment*, Vol. 6, 2020. https://doi.org/10.3389/fbuil.2020.00102.

[41] Jingqiao Zhang, and Sanderson, A., "JADE: Adaptive Differential Evolution With Optional External Archive," *IEEE Transactions on Evolutionary Computation*, Vol. 13, No. 5, 2009, pp. 945–958. https://doi.org/10.1109/TEVC.2009.2014613.

3

Conclusions and Recommendations

The goal of this research is to design planar Lyapunov orbits around the colinear Lagrange points of the Alpha Centauri system. By changing the lightness number and the true anomaly of the system at the start of the Lyapunov orbit, multiple sets of families of Lyapunov orbits are designed. This is done to investigate the effects of these parameters on the dynamics in the system. The designed periodic orbits are then used to make an initial design for a trajectory between two Lyapunov orbits with the use of an adaptive differential evolution. This trajectory can be improved with the use of a multiple shooting differential correction algorithm in future research. In Section 3.1, the research question which are given in Chapter 1 are answered. The results of the work are then used to give recommendations on future work in Section 3.2.

3.1. Conclusion

The conclusions of the research are drawn by answering the research questions in Chapter 1.

1. What kind of planar Lyapunov orbits exist around the colinear Lagrange points in the Alpha-Cen system using photon-pressure acceleration?

There are many families of planar Lyapunov orbits in the Alpha Centauri system. Due to the eccentricity, the period of each Lyapunov orbit is constraint to be 2π, or a fraction of that. For the L_2 and L_3 points, there are only Lyapunov orbits with a period of 2π. This means that the orbit of the photon sail around the Lagrange point has the same period as the orbits of Alpha Centauri A and B. In the case of Lyapunov orbits around L_1, there exist orbits with a period of 2π and π. The latter passes through the axis between Alpha Centauri A and B twice as much as compared to the orbit with a period of 2π. Both orbits around the L_1 point stay in between Alpha Centauri A and B and have a smaller trajectory. Due to the eccentricity of the system, the equations of motion depend on the true anomaly of the system. Therefore, there is an infinite amount of Lyapunov orbits available depending on the moment when the orbit starts. In this paper, two moments are investigated at which the orbit starts. The true anomaly at these moments θ_0 has been chosen to be 0 and π. The designed Lyapunov orbits are used to answer the subquestions as well.

- How do these Lyapunov orbits change when varying the lightness number of the photon-sail?

There are four different sets of periodic orbits considered in this research. One set around L_2, one around L_3 and two around L_1. Each set consists of two true anomalies at the start of the orbit and each true anomaly consists of a set of 5 constant steering laws. This results in 40 different families of periodic orbits with different maximum lightness numbers. For each orientation, the maximum lightness number is shown in Table 3.1. Depending on the orientation, the Lyapunov orbit behaves in three ways when the lightness number is increased, which is visualised in this table as well.

In some cases, the larger photon-pressure acceleration causes the photon sail to slow down, creating a smaller trajectory. If the sail is orientated in such a way that the emitted photons keep decreasing the spacecraft, the Lyapunov orbit converges towards an AEP. The maximum lightness number is the same

Table 3.1: Maximum achievable lightness number of PRP-augmented Lyapunov orbits for different constant steering laws. Table is colored where Green: $\beta = 2$, Blue: $V_{max} \to 0$ and Yellow: $V_{max} \to \infty$

Lagrange Point (T_1)	$\theta_0 = 0$					$\theta_0 = \pi$				
	α_A [deg]		α_B [deg]			α_A [deg]		α_B [deg]		
	0	90	0	90	$\hat{n} = [0\ 1\ 0]$	0	90	0	90	$\hat{n} = [0\ 1\ 0]$
L_1 (2π)	0,727	0,6188	1,0252	2	2	0,7276	2	0,9302	0,1903	2
L_1 (π)	0,7277	2	1,0544	2	2	0,7277	2	0,9032	2	2
L_2	0,2661	0,2091	1,8641	0,1131	0,1353	0,6739	2	1,8628	0,5596	2
L_3	0,7272	0,2444	0,844	0,0631	0,0539	0,7274	1,4528	0,7275	2	0,2773

as the lightness number required to create an AEP close to a star. If the Lyapunov orbit converges towards α-Cen A, the maximum lightness number is 0.727 and if it converges towards α-Cen B, this value is approximately 1.86. This first option is shown in the blue cells in Table 3.1. The second option is that the sail is oriented in such a way that the spacecraft is slowed down again. However, once the orbit becomes smaller, the spacecraft stays in between the two stars, which makes it possible to orient the sail in such a way that only a limited amount of PRP acceleration is present. This causes the Lyapunov orbit to become (almost) independent to the lightness number once the orbit is small enough. These orientations reach the defined maximum lightness number of 2, which are shown in green in Table 3.1. Lastly, the PRP acceleration can speed up the spacecraft. This causes the Lyapunov orbit to become larger for an increased lightness number in the ER3BP. These larger orbits have an higher maximum velocity as it orbits closer to the stars. Eventually, the maximum velocity tends to go to infinity. The maximum achievable lightness number is reached at this vertical asymptote. These maximum velocities are shown in yellow in Table 3.1.

- What is the effect of the initial true anomaly on these Lyapunov orbits?

Due to the fact that the start of the orbit is defined at the closest point to the star on the axis through Alpha Centauri A and B, the initial true anomaly θ_0 has a big influence on the Lyapunov orbits. Especially in the case of orbits around L_2 and L_3 as these orbit relatively close to the stars. In the pulsating frame, the position vector stays constant for a varying true anomaly, but the position is maximum at a true anomaly of π in the non-pulsating frame. Therefore, the relative distance to the star is maximised by setting the initial true anomaly at π. In the case of $\theta_0 = 0$, no orientation reaches the maximum lightness number for Lyapunov orbits around L_2 and L_3. If $\theta_0 = \pi$, in total 3 of the 10 orientations reach the maximum lightness number. For orbits around L_1, this does not have a great influence, as the number of orientations that reach the maximum lightness number is the same for both values of θ_0.

A set of two periodic orbits is used to investigate the possibility of designing a trajectory between these Lyapunov orbits. This is used to answer the last research question

1. Is it possible to travel between the designed Lyapunov orbits in the α-Cen system using photon-pressure acceleration?

With the use of an adaptive differential evolution algorithm, an initial trajectory between the Lyapunov orbits has been investigated. This is done between a Lyapunov orbit around L_2 and L_3 to fully explore the Alpha Centauri stem. The algorithm minimises the Euclidean error between the final states of a departure and an arrival leg. Three different lightness numbers have been used to design these trajectories, $\beta = 0.1$, 0.5, and 2. The trajectory with a lightness number of 0.1 had a remaining dimensionless Euclidean error in the range of 1E-1 to 1E-3, depending on the chosen Lyapunov orbits. The larger lightness numbers achieve a Euclidean error in the range of 1E-8. Therefore, it can be assumed that the trajectory is continuous, so it is possible to travel between the Lyapunov orbits to further explore Alpha Centauri.

3.2. Recommendations

Identifying the planar Lyapunov orbits around the colinear Lagrange points in Alpha Centauri is the next step in investigating the dynamics in this system. However, much more can be investigated on the

basis of this research. First, in this paper, five different constant orientations have been investigated. These orientations are the limits of the sail, as the cone angles were set to 0 or 90 deg. To further investigate the effect of the cone angle, a broader set of orientations should be used. The tipping points between converging to an AEP or reaching the maximum lightness number can be of great interest. The same can be said of the initial true anomalies. Again, the two boundary conditions have been observed, $\theta_0 = 0$ and π, but the range in between has not been investigated. The tipping points in this range can also provide insight into the dynamics.

In addition, different sets of periodic orbits can be researched in the future as well. For example, vertical Lyapunov or halo orbits can be designed. Next, the periodic orbits around the triangular Lagrange points can be investigated. This does not limit to Alpha Centauri, but this method can be used for any binary (stellar) system. This paper has focused on Alpha Centauri, but by changing the eccentricity, the dimensionless mass parameter, and the luminosity of the stars, any stellar system can be investigated. It not only limits two binary stellar systems, but can also be used to improve the photon-sail dynamics in the Solar System by adding the luminosity of the gas giants.

It is also recommended to further improve the dynamical model in this paper. An example of such an improvement could be to include the addition of eclipses. For now, the emitted photons could reach the sail at any point. However, the photons cannot pass through the other star in reality. Another example is to include a more realistic model of the photon sail in comparison to the ideal sail.

A recommendation for further research on the trajectories between the Lyapunov orbit is to optimise the trajectories. This can be done by decreasing the time of flight of the trajectories using an MSDC. By constraining the TOF and using the continuation method to slowly decrease this TOF, a more optimal solution can be found. Besides that, the physical trajectory can also be optimised. For example, an optimal solution could be to maximise the fraction of time spent in the habitable zone of Alpha Centauri.

A

Verification and Validation

This section is added to show the process of ensuring that the model is implemented correctly. This is done for the dynamical model, the photon-sail model, the method to find periodic orbits and lastly the method to find trajectories between the periodic orbits.

A.1. Dynamical model

The dynamical model is mainly based on the equations of motions (EoMs) of the elliptical restricted three-body problem, the photon-sail model and the state transition matrix (STM). These three models are verified to ensure that the models are implemented correctly.

A.1.1. Equations of motion

The dynamical model is based on the equations of motion. To verify the implementation of the dynamical model, the method to find the Lagrange points are investigated. First, the triangular Lagrange points can be easily verified as they form an equilateral triangle with the two primary bodies. The colinear Lagrange points can be verified using the literature from Ref. [32]. In this book, the colinear Lagrange points are given for varying values of μ. For three different values of μ, the outcome of the model is checked with the given values in Ref. [32]. For values of $\mu = 0.000001$, $\mu = 0.1$ and $\mu = 0.49$, it has been verified that the correct locations of the Lagrange points have been found.

A.1.2. Photon-sail model

The second step will be two verify the implementation of the photon sail model. This is done by displacing the classical Lagrange points using a photon sail. This has been investigated before in Ref. [1] and the results are shown in Figure A.1. Here, the required lightness number is displayed by the colour of the contour lines in the plots. The left side corresponds to the possible equilibrium points for a photon sail with one reflective side, while the right plot corresponds to a two sided reflective sail.

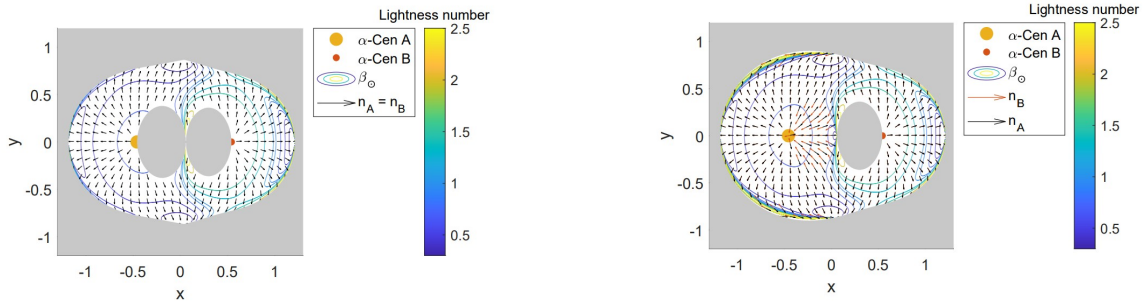

(a) One-sided sail

(b) Two-sided sail

Figure A.1: Required lightness number for artificial equilibrium point in the α-Cen system from literature [1]

By recreating these plots, the implementation of the photon sail acceleration can be verified. In Figure A.2, it can be seen that the contour plots are exactly the same as in the literature. The photon sail model does not only consist of the acceleration, but also the orientation of the sail. The arrows in the plots correspond to the orientation of the sail. Both plots are similar to the ones in the literature when comparing the orientation of the sail.

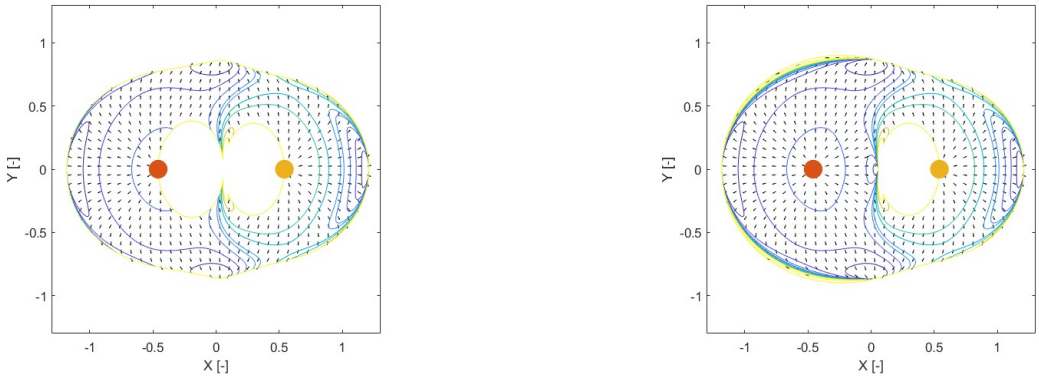

(a) One-sided sail

(b) Two-sided sail

Figure A.2: Required lightness number for artificial equilibrium point in the α-Cen system

A.1.3. State transition matrix

Next to the artificial equilibrium points, the monodromy matrix is verified to check the STM of the dynamical model. The monodromy matrix is used to investigate the stability of the system [1]. By integrating the STM over the period of the system, so $\Phi(\theta_0 + 2\pi, \theta_0)$, the monodromy matrix is found. The eigenvalues λ of the monodromy matrix characterize the stability of the system. If the eigenvalues satisfy $|\lambda| \leq 1$, the system is stable. For a small Δ, the system is said to be almost stable if the eigenvalues satisfy $|\lambda| \leq 1 + \Delta$. If this is not the case, the system is determined to be unstable. The stability of the α-Cen system, which is modeled using the ER3BP has been researched before [1]. In Figure A.3, the stability of the equilibrium points are shown. Here, the light-gray regions are infeasible for AEPs, which have been shown in Figure A.2 as well. The black regions are unstable equilibrium points. In Figure A.4, the linear stability is shown for a one-sided sail. Hereby the state transition matrix is verified to have been implemented correctly.

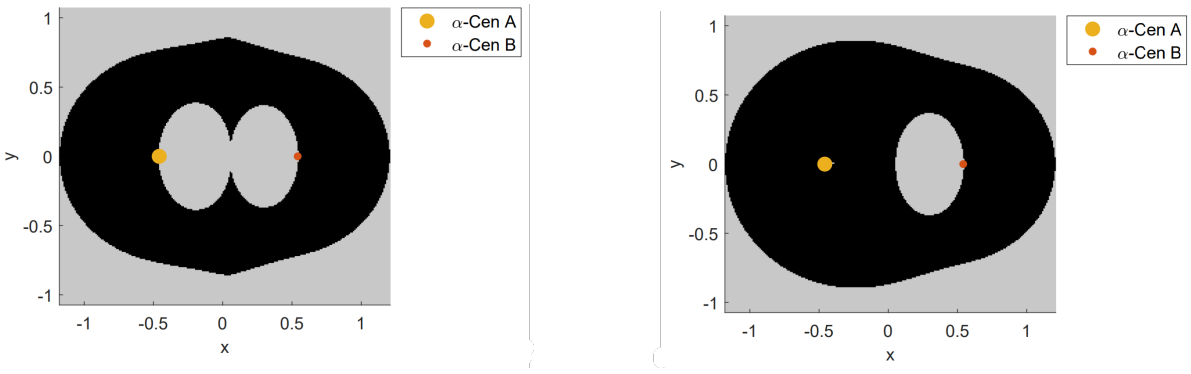

(a) One-sided sail

(b) Two-sided sail

Figure A.3: Linear stability of the equilibria in the α-Cen system, where white = stable, dark-gray = almost stable, black = unstable and light-gray = infeasible [1]

A.2. Periodic orbits

To verify the method of designing periodic orbits, the results of the method are verified using previously designed periodic orbits in the CR3BP [2], the PRP-augmented CR3BP [33] and the ER3BP [31]. In

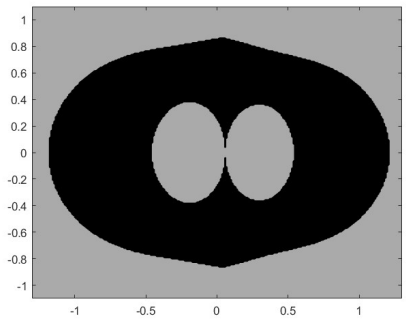

Figure A.4: Linear stability of the equilibria in the α-Cen system for a one-sided sail

Figure A.5, a family of Lyapunov orbits in the CR3BP of the Earth-Moon system[2]. In Figure A.5a, the trajectories are shown and in Figure A.5b, the periods of these trajectories are shown. In Figure A.6, a recreation of the family of orbits is made to verify whether the model is implemented correctly. Both the trajectories and periods of these orbits are similiar to the ones in the literature. Therefore, it is verified that the MSDC is implemented correctly to find periodic orbits in the CR3BP.

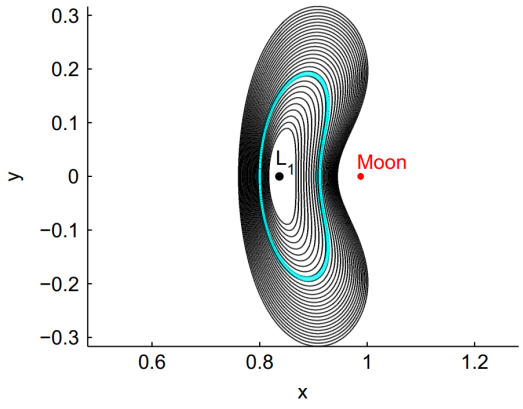

(a) Trajectories of the family of orbits

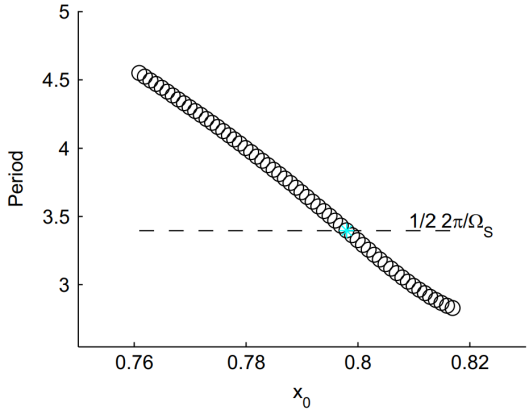

(b) Periods of the family of orbits

Figure A.5: Lyapunov orbits around L_1 in the CR3BP of the Earth-Moon system from literature [2]

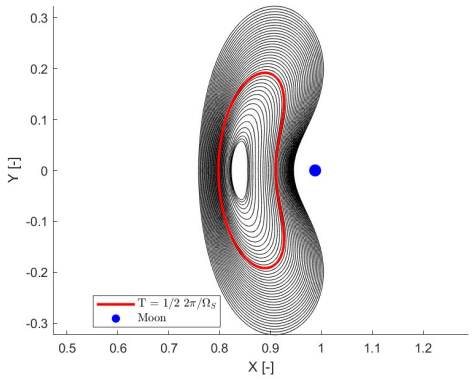

(a) Trajectories of the family of orbits

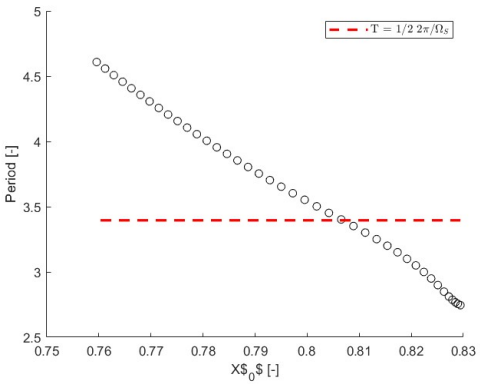

(b) Periods of the family of orbits

Figure A.6: Lyapunov orbits around L_1 in the CR3BP of the Earth-Moon system

The next step is to verify the photon-pressure acceleration model to find PRP-augmented periodic orbits. In Figure A.7a, a family of Lyapunov orbits around the L_1 point in the PRP-augmented

CR3BP of the Sun-Earth system are shown [33]. In Figure A.7b, the recreated family using the MSDC algorithm is shown. Here, the recreated orbits have the same trajectories compared to the trajectories in the literature. Therefore, it is verified that the PRP acceleration is implemented correctly.

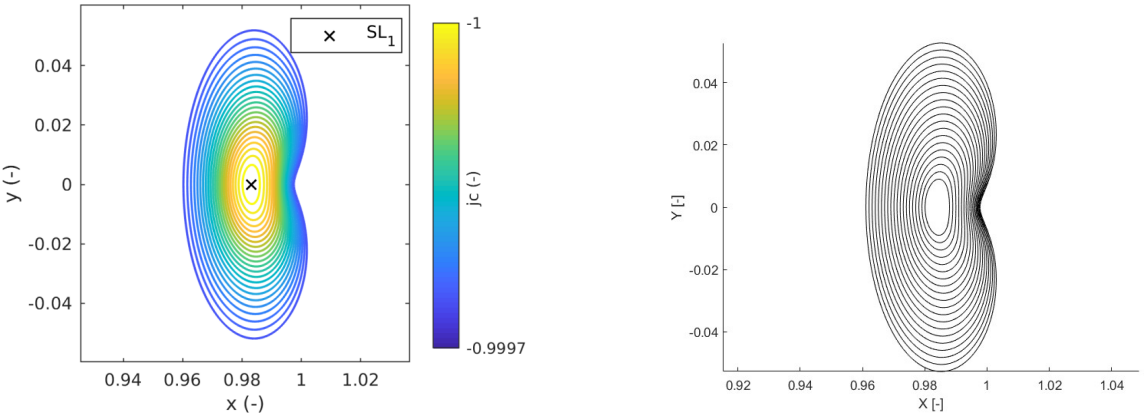

(a) Family of orbits from literature [33]

(b) Recreated family of orbits with MSDC

Figure A.7: Family of PRP-augmented Lyapunov orbits

The last step of verifying the method to find periodic orbits in α-Cen is to verify whether the method works in the ER3BP as well. In literature, the difference between periodic orbits in CR3BP and ER3BP in the Earth-Moon system are identified for the L_1 and L_2 point. These are shown in Figure A.8 and A.10a, respectively [3],[31]. In Figure A.8, the effect of varying the true anomaly at the start of the orbit is shown as well. Using the MSDC algorithm, the orbits around L_1 and L_2 are recreated as is shown in Figures A.9 and *A.10b*. These are the same as the orbits from the literature and therefore the model is verified to work correctly.

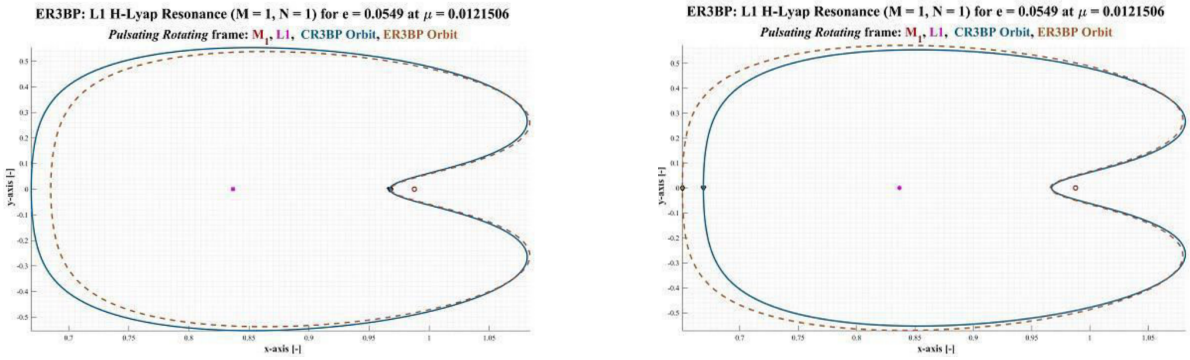

(a) Periodic orbit with $\theta_0 = 0$

(b) Periodic orbit with $\theta_0 = \pi$

Figure A.8: Periodic orbits in the ER3BP (Orange) and CR3BP (Blue) around the L_1 point of the Earth-Moon system from literature [3]

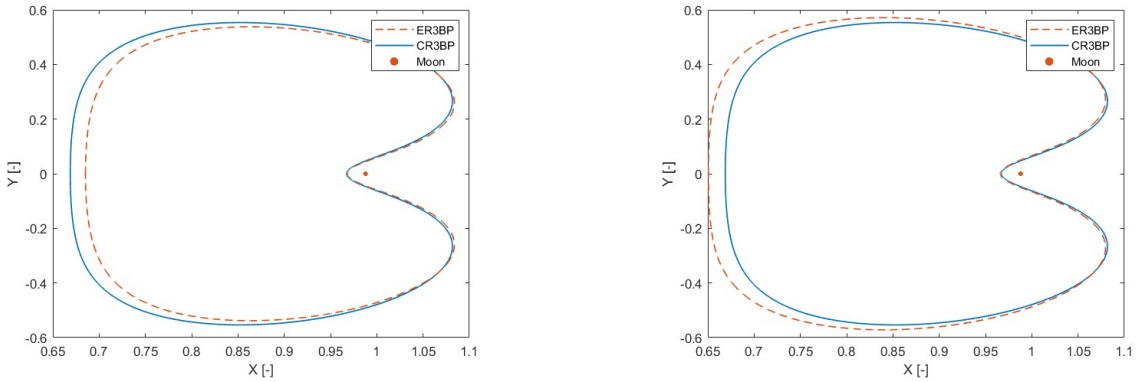

(a) Periodic orbit with $\theta_0 = 0$

(b) Periodic orbit with $\theta_0 = \pi$

Figure A.9: Periodic orbits in the ER3BP (Orange) and CR3BP (Blue) around the L_1 point of the Earth-Moon system

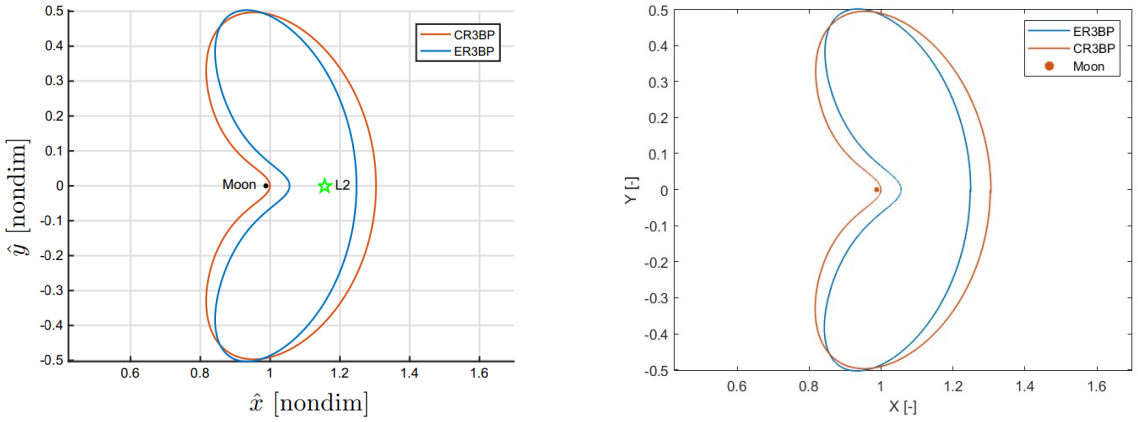

(a) Lyapunov orbits from literature [31]

(b) Recreated Lyapunov orbits

Figure A.10: Planar lyapunov orbits around L_2 in CR3BP (red) and ER3BP (blue) in the Earth-Moon system

B

Plots of planar Lyapunov orbits with maximum lightness number

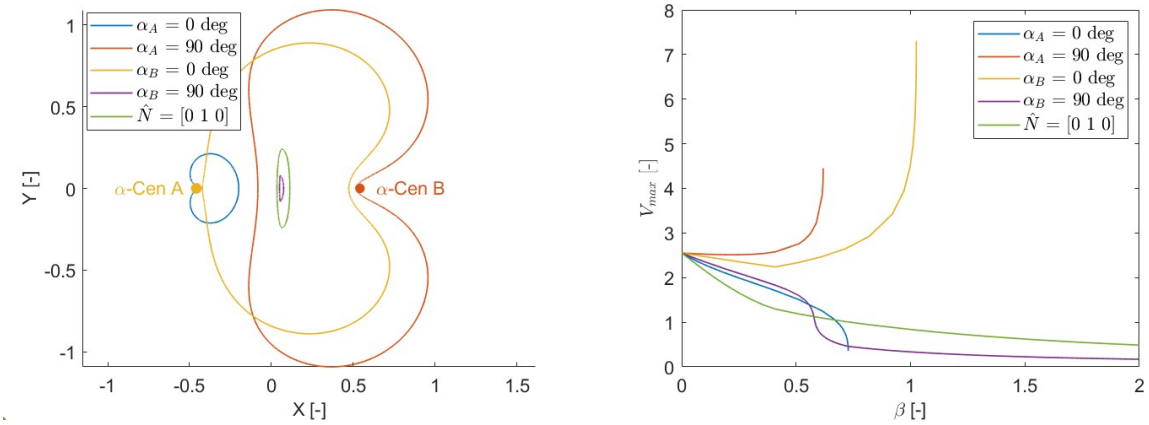

(a) Lyapunov orbits for achieved β_{max}

(b) V_{max} for increasing lightness number

Figure B.1: PRP-augmented Lyapunov orbits around L_1 with $T_1 = 2\pi$ and $\theta_0 = 0$

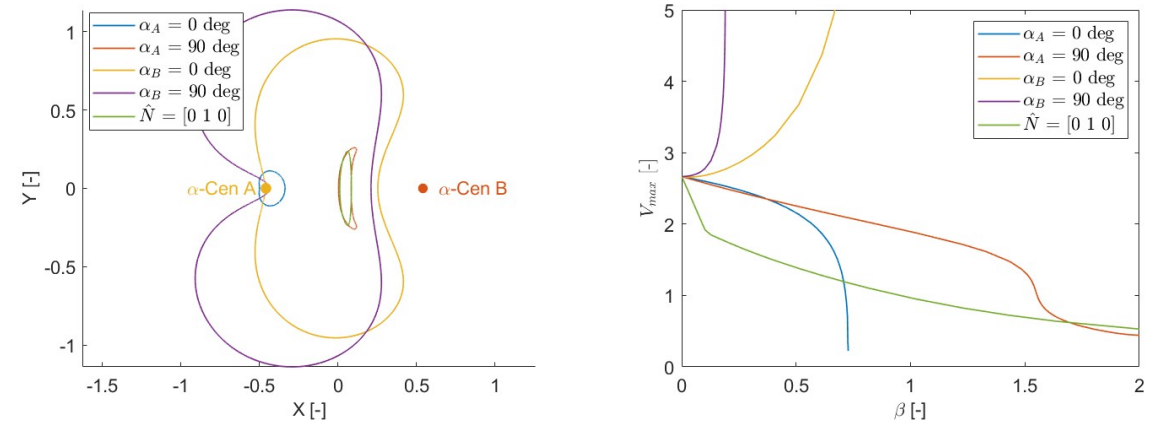

(a) Lyapunov orbits for achieved β_{max}

(b) V_{max} for increasing lightness number

Figure B.2: PRP-augmented Lyapunov orbits around L_1 with $T_1 = 2\pi$ and $\theta_0 = \pi$

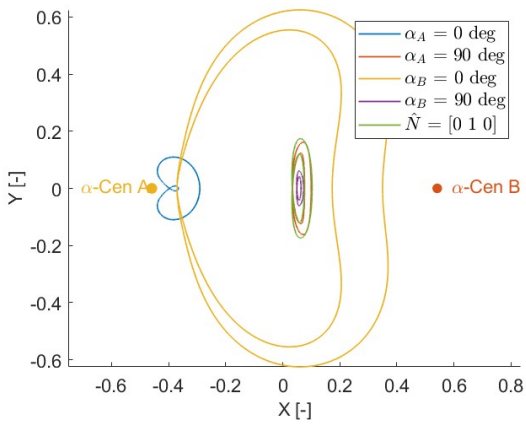

(a) Lyapunov orbits for achieved β_{max}

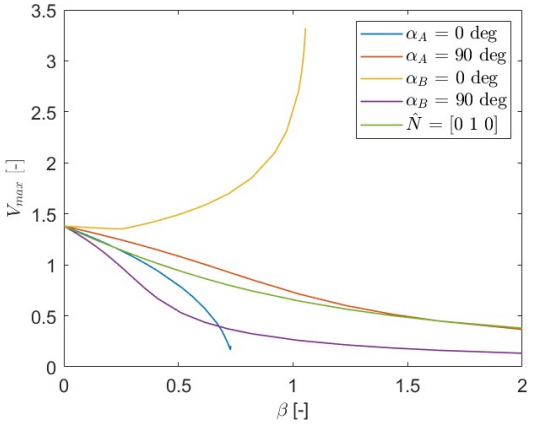

(b) V_{max} for increasing lightness number

Figure B.3: PRP-augmented Lyapunov orbits around L_1 with $T_1 = 1\pi$ and $\theta_0 = 0$

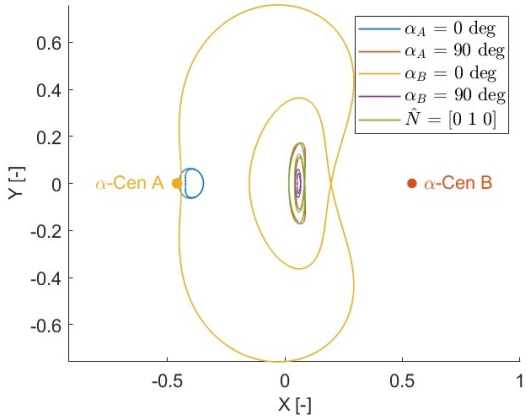

(a) Lyapunov orbits for achieved β_{max}

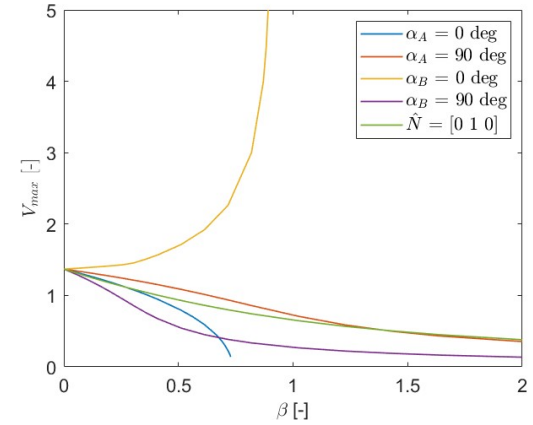

(b) V_{max} for increasing lightness number

Figure B.4: PRP-augmented Lyapunov orbits around L_1 with $T_1 = 1\pi$ and $\theta_0 = \pi$

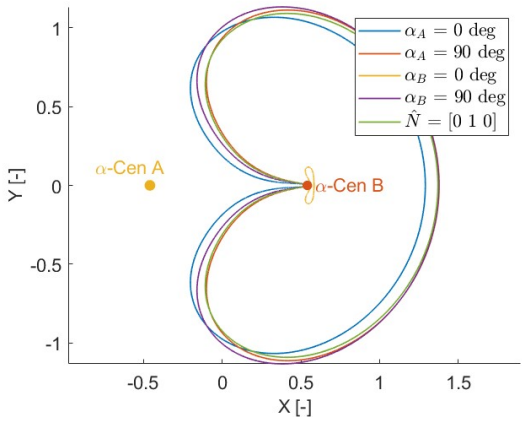

(a) Lyapunov orbits for achieved β_{max}

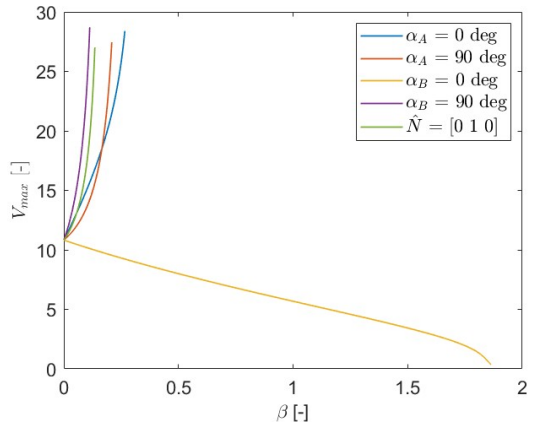

(b) V_{max} for increasing lightness number

Figure B.5: PRP-augmented Lyapunov orbits around L_2 with $\theta_0 = 0$

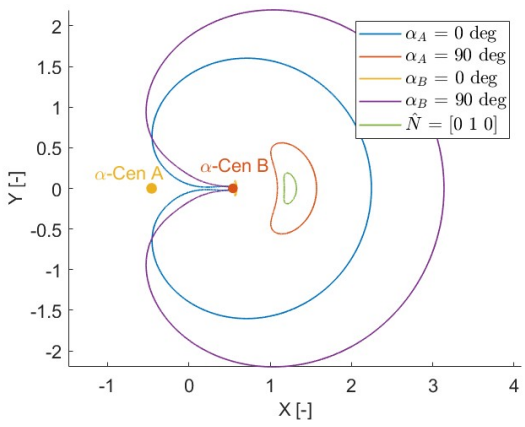

(a) Lyapunov orbits for achieved β_{max}

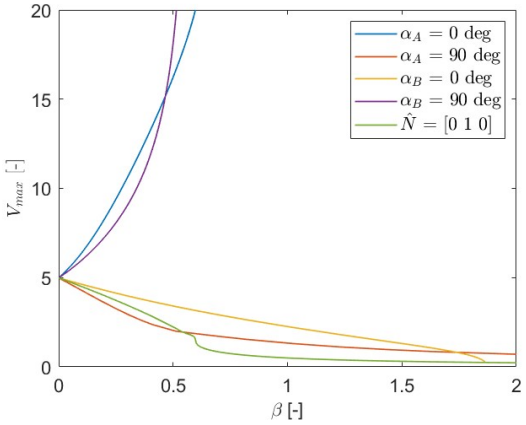

(b) V_{max} for increasing lightness number

Figure B.6: PRP-augmented Lyapunov orbits around L_2 with $\theta_0 = \pi$

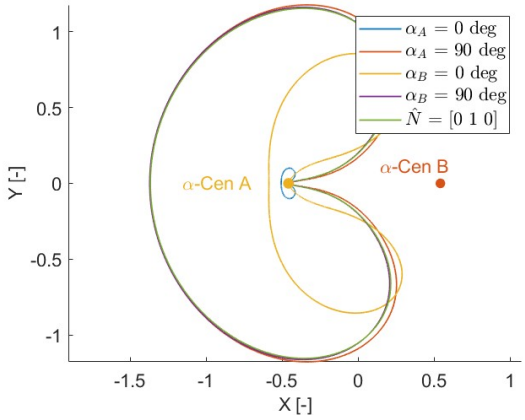

(a) Lyapunov orbits for achieved β_{max}

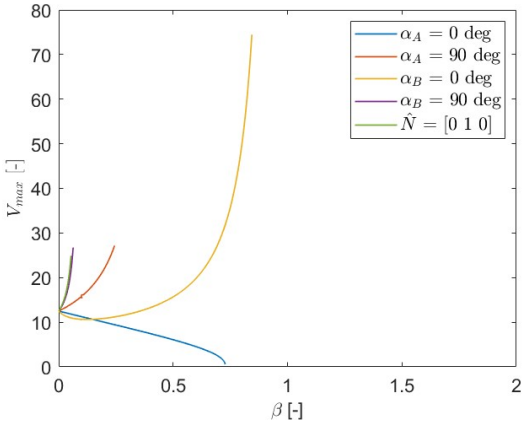

(b) V_{max} for increasing lightness number

Figure B.7: PRP-augmented Lyapunov orbits around L_3 with $\theta_0 = 0$

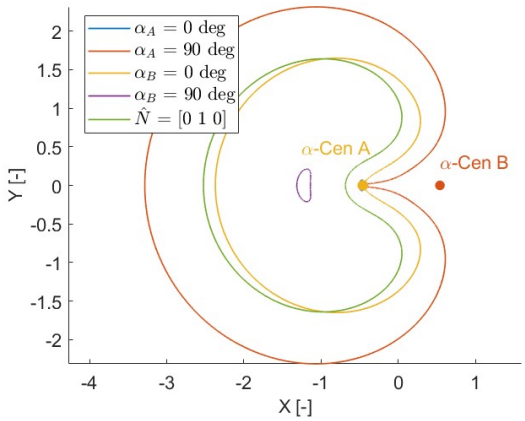

(a) Lyapunov orbits for achieved β_{max}

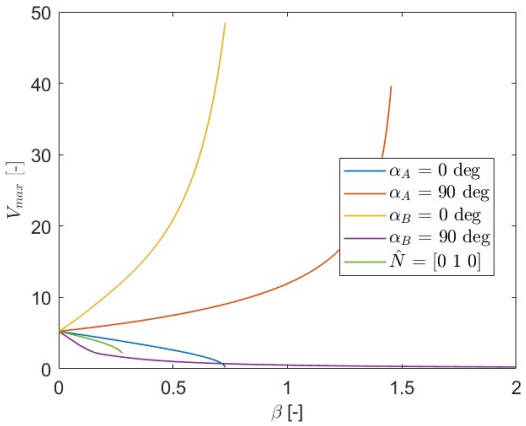

(b) V_{max} for increasing lightness number

Figure B.8: PRP-augmented Lyapunov orbits around L_3 with $\theta_0 = \pi$

Bibliography

[1] Jeannette Heiligers, Frederic Schoutetens, and Bernd Dachwald. Photon-Sail Equilibria in the Alpha Centauri System. Journal of Guidance, Control, and Dynamics, 44(5):1053–1061, 5 2021.

[2] Jeannette Heiligers, Sander Hiddink, Ron Noomen, and Colin R. McInnes. Solar sail Lyapunov and Halo orbits in the EarthMoon three-body problem. Acta Astronautica, 116:25–35, 11 2015.

[3] L. Massarweh. Linear stability and bifurcations of periodic Lagrange orbits in the Elliptic Restricted 3-Body Problem. PhD thesis, Aerospace Engineering, Delft University of Technology, 2016.

[4] J. Clerk Maxwell. A Dynamical Theory of the Electromagnetic Field. Philosophical Transactions of the Royal Society of London, 155:459–512, 1865.

[5] Urbanczyk. Solar sails - a Realistic Propulsion for Spacecraft. Astronautyka, 8(3):20–23, 8 1965.

[6] Louis Friedman. Starsailing: Solar Sails and Interstellar Travel. Wiley, first edition, 1 1988.

[7] Osamu Mori, Hirotaka Sawada, Ryu Funase, Mutsuko Morimoto, Tatsuya Endo, Takayuki Yamamoto, Yuichi Tsuda, Yasuhiro Kawakatsu, Jun'ichiro Kawaguchi, Yasuyuki Miyazaki, Yoji Shirasawa, Demonstration Team, and IKAROS Solar Sail W. First Solar Power Sail Demonstration by IKAROS. Transactions of the Japan Society for Aeronautical and Space Sciences, Aerospace Technology Japan, 8(27):425–431, 2010.

[8] Giovanni Vulpetti, Les Johnson, and Gregory L. Matloff. The NanoSAIL-D2 NASA Mission. In Solar Sails, pages 173–178. Springer New York, New York, NY, 2015.

[9] David A. Spencer, Bruce Betts, John M. Bellardo, Alex Diaz, Barbara Plante, and Justin R. Mansell. The LightSail 2 solar sailing technology demonstration. Advances in Space Research, 67(9):2878–2889, 5 2021.

[10] Yuichi Tsuda, Osamu Mori, Ryu Funase, Hirotaka Sawada, Takayuki Yamamoto, Takanao Saiki, Tatsuya Endo, Katsuhide Yonekura, Hirokazu Hoshino, and Jun'ichiro Kawaguchi. Achievement of IKAROS Japanese deep space solar sail demonstration mission. Acta Astronautica, 82(2):183–188, 2 2013.

[11] Martin Beech. Alpha Centauri. Springer International Publishing, Cham, 2015.

[12] N. Kameswara-Rao, A. Vagiswari, and C. Louis. Father J. Richaud and Early Telescope Observations in India. Bulletin of the Astronomical Society of India, 12(1):81–81, 3 1984.

[13] R.T.A. Innes. A Faint Star of Large Proper Motion. Circular of the Union Observatory Johannesburg, 30:235–236, 10 1915.

[14] P. Kervella, F. Thévenin, and C. Lovis. Proximas orbit around α Centauri. Astronomy & Astrophysics, 598:L7, 2 2017.

[15] Guillem Anglada-Escudé, Pedro J. Amado, John Barnes, Zaira M. Berdiñas, R. Paul Butler, Gavin A. L. Coleman, Ignacio de la Cueva, Stefan Dreizler, Michael Endl, Benjamin Giesers, Sandra V. Jeffers, James S. Jenkins, Hugh R. A. Jones, Marcin Kiraga, Martin Kürster, Mara J. López-González, Christopher J. Marvin, Nicolás Morales, Julien Morin, Richard P. Nelson, José L. Ortiz, Aviv Ofir, Sijme-Jan Paardekooper, Ansgar Reiners, Eloy Rodríguez, Cristina Rodrguez-López, Luis F. Sarmiento, John P. Strachan, Yiannis Tsapras, Mikko Tuomi, and Mathias Zechmeister. A terrestrial planet candidate in a temperate orbit around Proxima Centauri. Nature, 536(7617):437–440, 8 2016.

[16] Mario Damasso, Fabio Del Sordo, Guillem Anglada-Escudé, Paolo Giacobbe, Alessandro Sozzetti, Alessandro Morbidelli, Grzegorz Pojmanski, Domenico Barbato, R. Paul Butler, Hugh R. A. Jones, Franz-Josef Hambsch, James S. Jenkins, María José López-González, Nicolás Morales, Pablo A. Peña Rojas, Cristina Rodríguez-López, Eloy Rodríguez, Pedro J. Amado, Guillem Anglada, Fabo Feng, and Jose F. Gómez. A low-mass planet candidate orbiting Proxima Centauri at a distance of 1.5 AU. Science Advances, 6(3), 1 2020.

[17] A. Suárez Mascareño, J. P. Faria, P. Figueira, C. Lovis, M. Damasso, J. I. González Hernández, R. Rebolo, S. Cristiani, F. Pepe, N. C. Santos, M. R. Zapatero Osorio, V. Adibekyan, S. Hojjatpanah, A. Sozzetti, F. Murgas, M. Abreu, M. Affolter, Y. Alibert, M. Aliverti, R. Allart, C. Allende Prieto, D. Alves, M. Amate, G. Avila, V. Baldini, T. Bandi, S. C. C. Barros, A. Bianco, W. Benz, F. Bouchy, C. Broeng, A. Cabral, G. Calderone, R. Cirami, J. Coelho, P. Conconi, I. Coretti, C. Cumani, G. Cupani, V. DOdorico, S. Deiries, B. Delabre, P. Di Marcantonio, X. Dumusque, D. Ehrenreich, A. Fragoso, L. Genolet, M. Genoni, R. Génova Santos, I. Hughes, O. Iwert, F. Kerber, J. Knusdstrup, M. Landoni, B. Lavie, J. Lillo-Box, J. Lizon, G. Lo Curto, C. Maire, A. Manescau, C. J. A. P. Martins, D. Mégevand, A. Mehner, G. Micela, A. Modigliani, P. Molaro, M. A. Monteiro, M. J. P. F. G. Monteiro, M. Moschetti, E. Mueller, N. J. Nunes, L. Oggioni, A. Oliveira, E. Pallé, G. Pariani, L. Pasquini, E. Poretti, J. L. Rasilla, E. Redaelli, M. Riva, S. Santana Tschudi, P. Santin, P. Santos, A. Segovia, D. Sosnowska, S. Sousa, P. Spanò, F. Tenegi, S. Udry, A. Zanutta, and F. Zerbi. Revisiting Proxima with ESPRESSO. Astronomy & Astrophysics, 639:A77, 7 2020.

[18] Charles Beichman, Marie Ygouf, Jorge Llop Sayson, Dimitri Mawet, Yuk Yung, Elodie Choquet, Pierre Kervella, Anthony Boccaletti, Ruslan Belikov, Jack J. Lissauer, Billy Quarles, Pierre-Olivier Lagage, Daniel Dicken, Renyu Hu, Bertrand Mennesson, Mike Ressler, Eugene Serabyn, John Krist, Eduardo Bendek, Jarron Leisenring, and Laurent Pueyo. Searching for Planets Orbiting Alpha Centauri A with the James Webb Space Telescope. 10 2019.

[19] Frederic Schoutetens, Bernd Dachwald, and Jeanette Heiligers. Optimisation of Photon-Sail Trajectories in the Alpha-Centauri System using Evolutionary Neurocontrol. In 7th International Conference on Astrodynamics Tools and Techniques, 1 2021.

[20] René Heller, Michael Hippke, and Pierre Kervella. Optimized Trajectories to the Nearest Stars Using Lightweight High-velocity Photon Sails. The Astronomical Journal, 154(3):115, 8 2017.

[21] René Heller and Michael Hippke. Deceleration of High-velocity Interstellar Photon Sails into Bound Orbits at α Centauri. The Astrophysical Journal, 835(2):L32, 2 2017.

[22] Generoso Aliasi, Giovanni Mengali, and Alessandro A. Quarta. Artificial equilibrium points for a solar balloon in the α Centauri system. Acta Astronautica, 104(2):464–471, 11 2014.

[23] Tommaso Pino and Christian Circi. A star-photon sailcraft mission in the Alpha Centauri system. Advances in Space Research, 59(9):2389–2397, 5 2017.

[24] Tim Rotmans. Photon sail trajectories to exoplanet Proxima b using heteroclinic connections. PhD thesis, Delft University of Technology, Delft, 2023.

[25] Daniel Grebow. Generating periodic orbits in the circular restricted three body problem with applications to lunar South pole coverage. PhD thesis, Purdue University, West Lafayette, 5 2006.

[26] Edson F. Goodrich. Numerical determination of short-period Trojan orbits in the restricted three-body problem. The Astronomical Journal, 71:88, 3 1966.

[27] K. C. Howell and H. J. Pernicka. Numerical determination of Lissajous trajectories in the restricted three-body problem. Celestial Mechanics, 41(1-4):107–124, 3 1987.

[28] Kenneth R. Lang. The Sun from Space. Springer Berlin Heidelberg, Berlin, Heidelberg, 2009.

[29] David Folta, T.A. Pavlak, Amanda Haapala, and Kathleen Howell. Preliminary design considerations for access and operations in Earth-Moon L1/L2 orbits. Advances in the Astronautical Sciences, 148:2073–2092, 1 2013.

[30] Ariadna Farrés and Àngel Jorba. Periodic and quasi-periodic motions of a solar sail close to SL 1 in the EarthSun system. Celestial Mechanics and Dynamical Astronomy, 107(1-2):233–253, 6 2010.

[31] Fabio Ferrari and Michèle Lavagna. Periodic motion around libration points in the Elliptic Restricted Three-Body Problem. Nonlinear Dynamics, 93(2):453–462, 7 2018.

[32] Victor Szebehely. Theory of Orbit; The restricted problem of three Bodies. Elsevier, 1967.

[33] Alvaro Fernandez Mora and Jeannette Heiligers. Solar-Sail Quasi-Periodic Orbits in the SunEarth System. Journal of Guidance, Control, and Dynamics, 43(9):1740–1749, 9 2020.